

An Adhesion-Dependent Switch between Mechanisms That Determine Motile Cell Shape

Erin L. Barnhart¹, Kun-Chun Lee², Kinneret Keren³, Alex Mogilner², Julie A. Theriot^{1,4*}

1 Department of Biochemistry and Howard Hughes Medical Institute, Stanford School of Medicine, Stanford, California, United States of America, **2** Department of Mathematics, University of California, Davis, California, United States of America, **3** Department of Physics and Russell Berrie Nanotechnology Institute, Technion – Israel Institute of Technology, Haifa, Israel, **4** Department of Microbiology and Immunology, Stanford School of Medicine, Stanford, California, United States of America

Abstract

Keratocytes are fast-moving cells in which adhesion dynamics are tightly coupled to the actin polymerization motor that drives migration, resulting in highly coordinated cell movement. We have found that modifying the adhesive properties of the underlying substrate has a dramatic effect on keratocyte morphology. Cells crawling at intermediate adhesion strengths resembled stereotypical keratocytes, characterized by a broad, fan-shaped lamellipodium, clearly defined leading and trailing edges, and persistent rates of protrusion and retraction. Cells at low adhesion strength were small and round with highly variable protrusion and retraction rates, and cells at high adhesion strength were large and asymmetrical and, strikingly, exhibited traveling waves of protrusion. To elucidate the mechanisms by which adhesion strength determines cell behavior, we examined the organization of adhesions, myosin II, and the actin network in keratocytes migrating on substrates with different adhesion strengths. On the whole, our results are consistent with a quantitative physical model in which keratocyte shape and migratory behavior emerge from the self-organization of actin, adhesions, and myosin, and quantitative changes in either adhesion strength or myosin contraction can switch keratocytes among qualitatively distinct migration regimes.

Citation: Barnhart EL, Lee K-C, Keren K, Mogilner A, Theriot JA (2011) An Adhesion-Dependent Switch between Mechanisms That Determine Motile Cell Shape. *PLoS Biol* 9(5): e1001059. doi:10.1371/journal.pbio.1001059

Academic Editor: Jonathan B. Alberts, University of Washington, United States of America

Received: December 23, 2010; **Accepted:** March 24, 2011; **Published:** May 3, 2011

Copyright: © 2011 Barnhart et al. This is an open-access article distributed under the terms of the Creative Commons Attribution License, which permits unrestricted use, distribution, and reproduction in any medium, provided the original author and source are credited.

Funding: ELB and JAT were supported by the Howard Hughes Medical Institute. KCL and AM were supported by NIH GLUE grant "Cell Migration Consortium" (NIGMS U54 GM64346) and NSF Grant DMS-0315782. KK was supported by grants from the European Research Council, the Morasha Program of the Israel Science Foundation and an Allon Fellowship from the Israel Council for Higher Education. The funders had no role in study design, data collection and analysis, decision to publish, or preparation of the manuscript.

Competing Interests: The authors have declared that no competing interests exist.

* E-mail: theriot@stanford.edu

Introduction

Motile cell shape and speed emerge from nanometer-scale interactions among constituent elements, including the actin network, myosin, adhesions, and the cell membrane [1]. Cell-substrate adhesion strength has a dramatic, biphasic effect on cell migration velocity: cell speed increases between low and intermediate adhesion strengths and decreases between intermediate and high adhesion strengths [2–5]. In addition, optimal adhesion strength for fast cell migration has been shown to depend on the level of myosin contraction, with cells crawling at faster speeds at low and high adhesion strengths when myosin activity is decreased or increased, respectively [3]. Thus, the balance between adhesion and myosin contraction clearly contributes to determining cell speed. However, the degree to which adhesion strength and myosin contraction may contribute to other properties of motile cells such as cell shape is poorly characterized.

Adhesion strength and myosin contraction have mechanical consequences that are likely to affect cell shape determination. Cells are thought to transmit forces to the underlying substrate via a mechanism in which adhesions act as “molecular clutches” that couple the actin network to the substrate [6]. This physical linkage creates a frictional slippage interface that balances myosin-mediated contractile forces [7–11]. According to this model, as the number of clutches increases, the friction coefficient increases,

increasing the amount of traction force that can be transmitted to the surface and slowing retrograde flow of the actin network. In contrast, as the amount of myosin contraction, and the amount of force transmitted by engaged clutches, increases, the off-rate constant for the clutches increases exponentially [12], reducing the average lifetime for the population of clutches. This effectively decreases the coefficient of friction between the cell and the substrate, reducing the amount of traction force that can be transmitted to the substrate and increasing actin retrograde flow. The dynamics of the cell boundary, and therefore cell shape, are determined in part by adhesion- and myosin-dependent friction and retrograde flow rates: high friction stabilizes actin-driven protrusion of the cell boundary, whereas low friction results in retrograde flow of the actin network and retraction of the cell boundary.

In addition to these mechanical effects, adhesion strength and myosin contraction affect organization of the actin network through a variety of signal transduction pathways [3]. Adhesions are complex, hierarchical structures: integrin molecules bind extracellular matrix proteins on the underlying surface, and many additional adhesion proteins, including proteins involved in signal transduction and actin binding proteins, recruit to adhesions on the inside of the cell [13]. Thus, these complex adhesions act as organizing centers, localizing biochemical signals that modify the organization of the actin network. For example, some evidence

Author Summary

Cell migration is important for many biological processes: white blood cells chase down and kill bacteria to guard against infection, epithelial cells crawl across open wounds to promote healing, and embryonic cells move collectively to form organs and tissues during embryogenesis. In all of these cases, migration depends on the spatial and temporal organization of multiple forces, including actin-driven protrusion of the cell membrane, membrane tension, cell-substrate adhesion, and myosin-mediated contraction of the actin network. In this work, we have used a simple cell type, the fish epithelial keratocyte, as a model system to investigate the manner in which these forces are integrated to give rise to large-scale emergent properties such as cell shape and movement. Keratocytes are normally fan-shaped and fast-moving, but we have found that keratocytes migrate more slowly and assume round or asymmetric shapes when cell-substrate adhesion strength is too high or too low. By correlating measurements of adhesion-dependent changes in cell shape and speed with measurements of adhesion and myosin localization patterns and actin network organization, we have developed a mechanical model in which keratocyte shape and movement emerge from adhesion and myosin-dependent regulation of the dynamic actin cytoskeleton.

suggests that nascent adhesions activate Rac GTPase [14], which promotes branching and polymerization of the actin network by activating Arp2/3 [15–17]. Mature adhesions, on the other hand, are thought to up-regulate RhoA GTPase activity [18,19], which promotes bundling of the actin network by activating the formin mDial1 [20]. RhoA also promotes myosin contraction by up-regulating myosin light chain kinase [21], and myosin contraction, in turn, promotes adhesion maturation [22–24], bundling of actin filaments [25], and actin depolymerization [26]. The manner in which mechanical and biochemical feedback among adhesions, myosin, and actin contributes to global actin network organization and cell shape determination is not well understood.

Fish epithelial keratocytes are an ideal model system for investigating cell shape determination [1,27,28]. Individual keratocytes maintain nearly constant shape, speed, and direction over many cell lengths of migration, but there is considerable heterogeneity within a population of keratocytes [29–33]. New methods for quantifying cell shape [34] have facilitated correlative studies of shape and actin network organization in large populations of keratocytes [29,30], resulting in a model for shape determination based on mechanical feedback between the treadmilling actin network and the inextensible cell membrane [29]. In this model, the polymerizing actin network pushes on the cell membrane from within, generating membrane tension that rapidly equilibrates and exerts globally constant force, per unit length, on the actin network. At the center of the leading edge, high actin filament density results in low membrane resistance per filament, allowing actin filaments to polymerize rapidly and drive protrusion of the leading edge. As the filament density decreases towards the cell sides, resistance per filament increases until the load due to membrane tension stalls actin polymerization, thereby setting the front corners of the cell. This model is consistent with experimental evidence that actin network densities are graded in fan-shaped keratocytes, but does not explicitly address the contributions of adhesions and myosin to the establishment of this graded actin filament distribution and overall cell shape.

In this work, we investigated the contributions of adhesion and myosin contraction to dynamic actin network organization and

keratocyte shape determination. We found that keratocyte shape and speed both have a biphasic dependence on adhesion strength; keratocytes crawling at intermediate adhesion strength are fast and fan-shaped, whereas keratocytes crawling at low and high adhesion strengths are slow and round. To elucidate the mechanism of adhesion-dependent shape determination, we examined actin network organization and dynamics, myosin localization, and adhesion distribution, as well as the consequences of myosin inhibition or activation, for cells plated at low, intermediate, or high adhesion strengths. We present a quantitative mechanical model in which adhesion-dependent actin polymerization and retrograde flow rates add vectorially at each point around the perimeter of the cell, determining cell shape. We find that as adhesion strength increases, cells undergo a qualitative switch in the mechanism of shape determination: at low adhesion strength, the pattern of actin retrograde flow is most important, while at high adhesion strength, the pattern of actin network growth becomes dominant. Overall, our mechanical model for cell shape determination is able to integrate the effects of all the known major relevant cellular components to generate quantitative predictions for large-scale cell behavior.

Results

Effects of Substrate Adhesivity on Keratocyte Shape and Movement

To determine the effect of adhesion strength on keratocyte motility, we modified the adhesive properties of the underlying substrate by using an Arg-Gly-Asp (RGD) functionalized poly-L-lysine-graft-(polyethylene glycol) copolymer (PLL-PEG-RGD) [35]. The positively charged PLL backbone of the copolymer binds negatively charged glass surfaces, the PEG chains prevent non-specific adsorption of serum proteins to the surface, and the RGD peptides promote specific cell adhesion via integrin binding [36,37]. Keratocytes were plated on glass surfaces coated with a range of RGD densities, where the RGD density was controlled by dilution of the PLL-PEG-RGD copolymer with a non-functionalized PLL-PEG copolymer. The strength of cell-substrate attachment increased with increasing PLL-PEG-RGD concentration, as expected (Figure S1), so for simplicity we refer to cells migrating on substrates coated with varying concentrations of PLL-PEG-RGD as migrating at various “adhesion strengths.” We found that keratocyte migration speed exhibited a biphasic dependence on adhesion strength (Figure 1C) similar to that previously observed in several slow-moving cell types [2–5]: cells plated at intermediate adhesion strengths migrated at faster speeds than cells plated at low and high adhesion strengths (0.16 $\mu\text{m/s}$ on surfaces coated with 4 $\mu\text{g/ml}$ PLL-PEG-RGD, compared to 0.12 and 0.11 $\mu\text{m/s}$ on surfaces coated with 0.8 and 500 $\mu\text{g/ml}$ PLL-PEG-RGD, respectively). Compared to other cell types, however, the dependence of keratocyte speed on adhesion strength was modest, with less than 50% change in migration speed across a wide range of adhesion strengths (Figure 1C).

In contrast to its modest effect on cell speed, we found that the adhesion strength of the underlying surface had a dramatic effect on cell morphology (Figures 1 and 2, Movies S1–S3). To quantify the effect of adhesion strength on cell shape, we first determined the principal modes of shape variation for large populations of cells plated on low, intermediate, and high RGD densities by principal component analysis of aligned outlines of live keratocytes (Figure 1B) [34]. The major shape modes for all three populations were similar to those previously measured for keratocytes plated on untreated glass coverslips [29]: the first two modes of variation were, roughly, the projected 2D area of the cell (mode 1), and cell

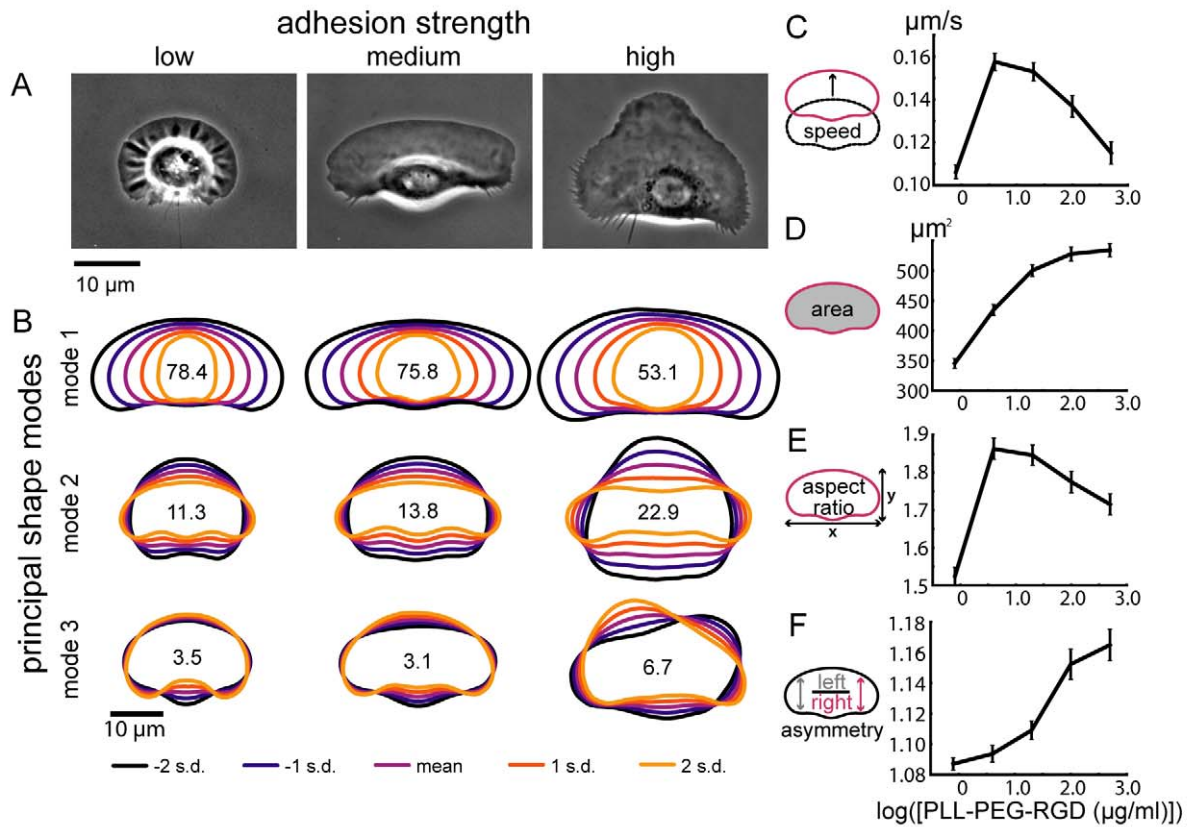


Figure 1. Adhesion strength of the underlying surface affects keratocyte migration speed and shape. (A) Phase contrast images of representative cells crawling at low (left), intermediate (center), and high (right) adhesion strengths (0.8, 4, and 500 $\mu\text{g/ml}$ PLL-PEG-RGD, respectively). (B) Principal modes of shape variation, as determined by principal component analysis of aligned cell outlines, are shown for populations of cells at low (left), intermediate (center), and high (right) adhesion strengths ($n > 200$ cells for each population). For each population of cells, the mean cell shape and shapes one and two standard deviations from the mean are shown for each shape mode. The variation accounted for by each mode is indicated. (C–F) Average cell speed (C), area (D), aspect ratio (E), and left-right asymmetry (F) are shown for live cells plated on surfaces coated with the indicated PLL-PEG-RGD concentrations. Error bars indicate standard error of the mean. doi:10.1371/journal.pbio.1001059.g001

aspect ratio, or cell width divided by cell length (mode 2). These two modes of shape variation accounted for approximately 90% of the total variation in the low and intermediate adhesion strength populations. In the high adhesion strength population, however, the first two modes accounted for less than 80% of the total variation, and a third shape mode, left-right asymmetry, accounted for an additional 6.7% of the variation. Based on these shape modes, we measured area, aspect ratio, and left-right asymmetry directly for keratocytes plated on a range of RGD densities (Figure 1D–1F). Area and left-right asymmetry increased with adhesion strength (Figure 1D, 1F), and aspect ratio exhibited a biphasic dependence on adhesion strength, with cells crawling at intermediate adhesion strength displaying the highest aspect ratios (Figure 1E). In addition, we examined shape variability (Figure S2) and leading edge dynamics (Figure 2) in individual cells. Although cells on low adhesion strength surfaces displayed more variable protrusion and retraction rates than cells on intermediate adhesion (Figure 2C–2E), both maintained persistent symmetrical shapes over long time periods with constant area and only slightly fluctuating aspect ratio and left-right asymmetry (Figure S2). While cells on high adhesion strength surfaces also maintained constant areas (Figure S2), they exhibited traveling waves of protrusion (Figure 2C–2E). In these cells, protrusion of the leading edge oscillated with periods ranging from 100 to 400 seconds, resulting in large oscillations in aspect ratio and left-right asymmetry (Figure S2).

To rule out the possibility that the observed adhesion-dependent migration behaviors were due to long-term adaptation to the different surfaces, we imaged individual cells as they crawled on micro-patterned surfaces, crossing from regions of low adhesion strength to regions of intermediate adhesion strength (Figure 3A–3F, Movie S4), and from regions of intermediate adhesion strength to regions of high adhesion strength (Figure 3G–3L, Movie S5). Area and aspect ratio increased immediately as cells crossed from low to medium adhesion strength regions (Figure 3D–3E), and speed decreased and waves of protrusion emerged as cells crossed from medium to high adhesion strength regions (Figure 3G–3I, 3L). Thus, changes in adhesion strength, in the absence of any long-term adaptation, are sufficient to switch keratocytes among three migration regimes: cells on low adhesion strength are small, round, and slow-moving; cells on intermediate adhesion strength surfaces are fan-shaped and fast-moving; and cells on high adhesion strength surfaces are large, slow-moving, and exhibit traveling waves of protrusion.

General Model for Keratocyte Shape Determination: Actin Polymerization and Retrograde Flow Control Cell Boundary Expansion and Retraction

We set out to develop a physical model for keratocyte shape determination that recapitulates the observed adhesion-dependent changes in steady-state cell shape. Our model builds on the graded

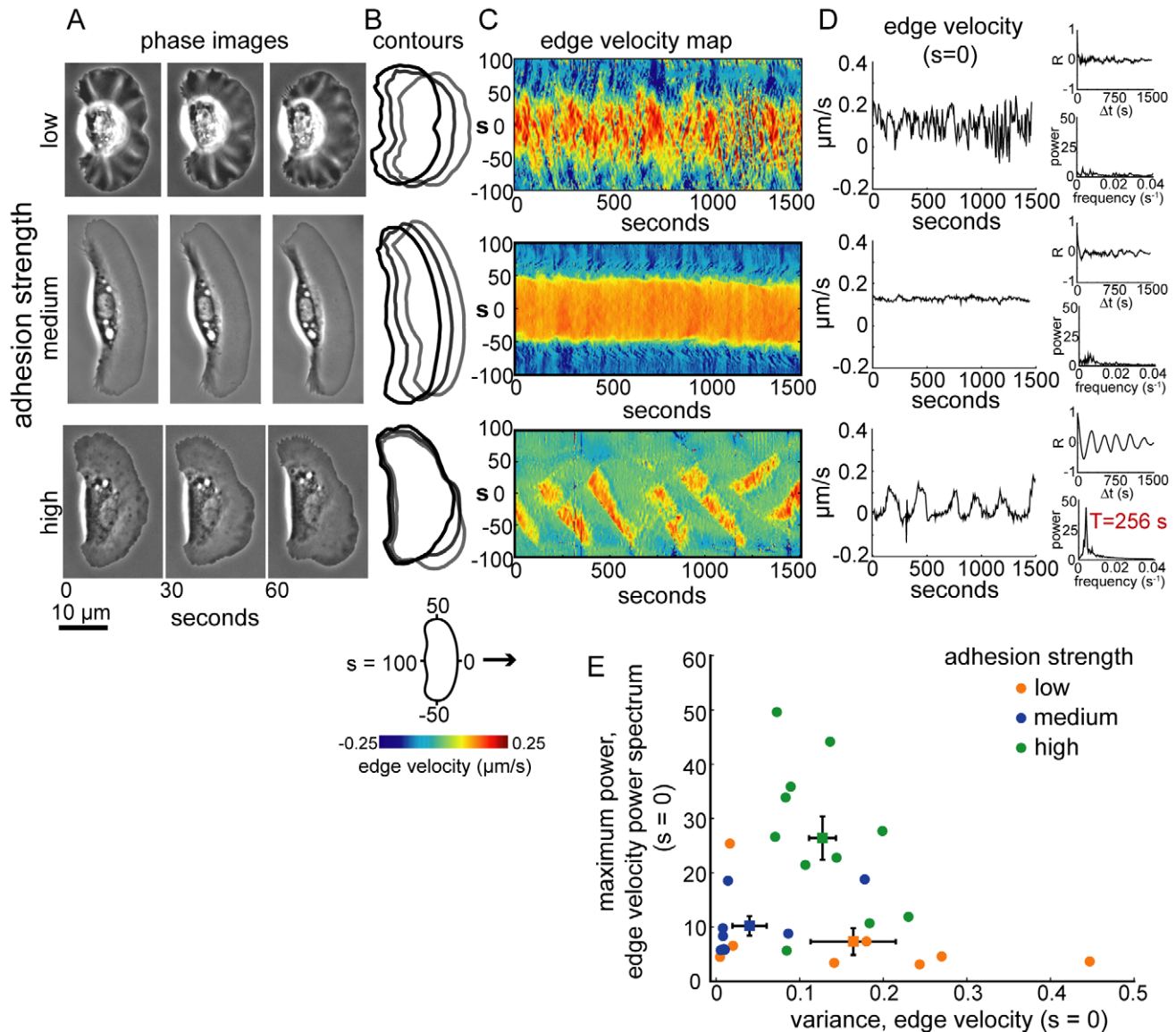


Figure 2. Oscillations in cell shape emerge as adhesion strength increases. (A–B) Phase contrast images (A) and cell contours (B) from representative cells crawling at low (top), intermediate (middle), and high (bottom) adhesion strength. (C) Edge velocity maps for each cell shown in (A). The velocity of the cell boundary at each point, s , around the cell perimeter is plotted over time. Hot colors represent protrusion of the cell boundary, and cold colors represent retraction. (D) Velocity of the cell boundary at the center of the leading edge ($s=0$) is plotted over time. The upper inset is the autocorrelation function for the edge velocity, and the lower inset is the power spectrum of the autocorrelation function. Velocity of the leading edge of the cell plated on the high adhesion strength surface oscillated with a period of 256 seconds. (E) The variance of the edge velocity at $s=0$ is plotted versus the maximum power in the edge velocity power spectrum for cells plated on low ($n=8$), intermediate ($n=8$), and high ($n=11$) adhesion strength surfaces. Squares represent the average values for each population; error bars indicate standard error of the mean. doi:10.1371/journal.pbio.1001059.g002

radial extension model for keratocyte motility, which proposes that local expansion of the cell boundary occurs perpendicular to the cell edge, with maximal rates of extension and retraction at the center of the leading and trailing edges, respectively, and minimal rates of expansion at the cell sides [27]. These expansion and retraction rates emerge from mechanical and biochemical feedback among adhesions, the treadmilling actin network, myosin, and the inextensible membrane. Specifically, we propose that at each point along the cell perimeter, actin polymerization and myosin II-driven retrograde flow of the actin network with respect to the underlying surface add vectorially to give the effective expansion/retraction rate: $v(s) = V_p(s) + U_{\perp}(s)$, where v is the expansion/retraction rate, V_p is the rate of actin

polymerization, U_{\perp} is the normal component of the centripetal bulk flow \vec{U} of the viscous F-actin network, and s is the position along the cell boundary, with $s=0$ at the center of the leading edge of the cell (Figure 4A). The actin network flows inward from the cell boundary, so U_{\perp} is negative. In order for a cell to migrate persistently, the molecular machinery that controls actin polymerization and retrograde flow must be organized such that actin polymerization is greater than retrograde flow in the front of the cell and retrograde flow is greater than polymerization in the rear of the cell (Figure 4B, 4D), with the cell corners set by the points where the rate of polymerization is equal to the rate of retrograde flow (Figure 4C). We propose that the rate of actin retrograde flow depends on the mechanical balance between myosin-mediated

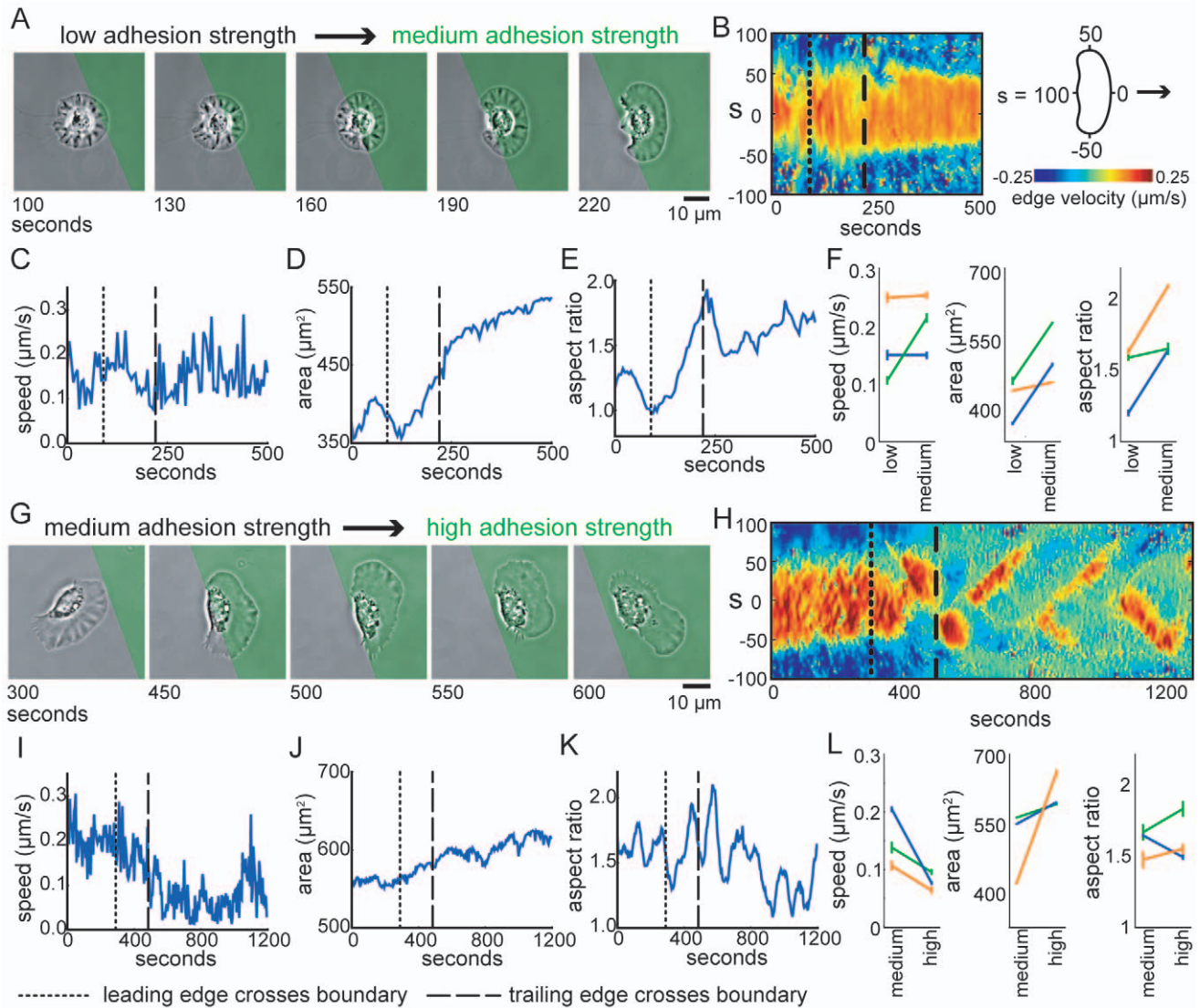


Figure 3. Individual cells transition between adhesion-dependent migration regimes. Cells crawling on micropatterned surfaces were imaged as they crossed boundaries between low and intermediate adhesion strength regions (A–F) and medium and high adhesion strength regions (G–L). (A,G) Phase images. The green overlay represents the region of medium (A) or high (G) adhesion strength. Edge velocity maps (B,H), cell velocity (C,I), area (D,J), and aspect ratio (E,K) are plotted over time for the cells shown in A and G. The dotted and dashed lines indicate when the leading and trailing edges crossed the boundaries, respectively. (F,L) Average cell speed, area, and aspect ratio are plotted for three cells before (left) and after (right) crawling from low to medium adhesion strength regions (F) or medium to high adhesion strength regions (L). Error bars indicate standard deviation for the individual cells.
doi:10.1371/journal.pbio.1001059.g003

contraction of the actin network and the adhesive forces that resist retrograde flow, and that the rate of actin polymerization depends on mechanical feedback between the actin network and the cell membrane. Sub-models for actin retrograde flow and actin polymerization are presented below. This mechanical model does not evoke any specific effects of adhesion-based signaling on actin cytoskeletal dynamics; instead it treats adhesion simply as a frictional force. Nonetheless, this simple model is sufficient to recapitulate our experimental observations on cell speed, shape, and protein distributions with remarkable accuracy.

Effects of Cell-Substrate Adhesion Strength on Actin Network Flow and Myosin Localization

The rate of retrograde actin network flow, \vec{U} , depends on the distribution of myosin-driven contractile forces, the viscosity of the

actin network, and the adhesive forces that resist contraction [38]. To compute \vec{U} , we used a model for viscous contractile flow of the lamellipodial actin network, adapted from [38]. In a simplified version of this model, the rate of the flow is determined by the balance between myosin contraction and adhesion strength (Figure 4B–4D): $\zeta \vec{U} = \nabla m$ gives the local contractile forces pulling on the adhesions, where ∇m is the gradient of the myosin-generated stress and ζ is the effective adhesion friction coefficient that quantifies the notion of the adhesion strength used to describe the experimental data. A complete model for actin network flow includes passive viscous stresses in the F-actin network (see Text S1). For simplicity, we assume that the adhesion drag coefficient ζ and F-actin viscosity are spatially constant and that myosin stress is isotropic and linearly proportional to the myosin density. To account for the myosin distribution, we assume that myosin binds

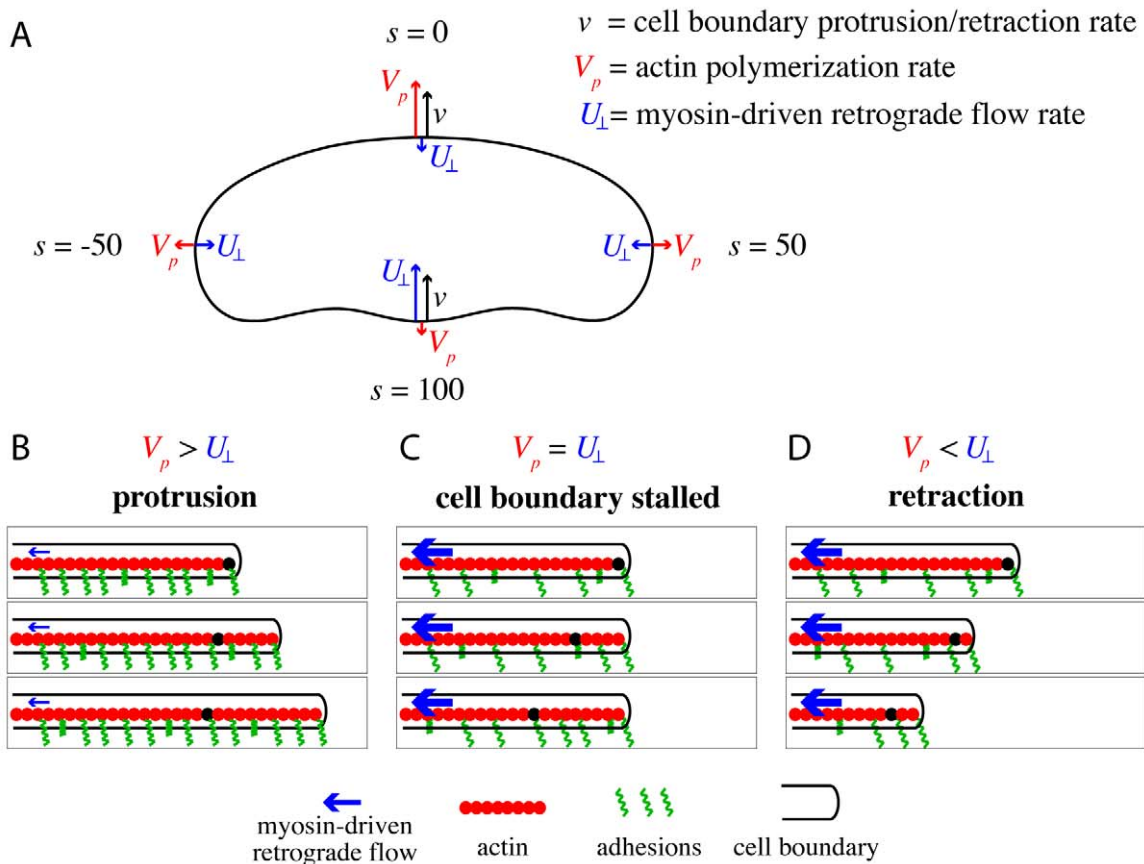


Figure 4. General model for keratocyte shape. (A) The expansion/retraction rate of the cell boundary is given by $v(s) = V_p(s) + U_{\perp}(s)$, where v is the expansion/retraction rate, V_p is the rate of actin polymerization, U_{\perp} is the normal component of the centripetal bulk flow \vec{U} of the viscous F-actin network, and s is the position along the cell boundary. In a migrating cell, the actin network, myosin, and adhesions must be organized such that V_p is greater than U_{\perp} at the front of the cell ($s=0$), and U_{\perp} is greater than V_p in the cell rear ($s=100$). The corners of the cell are defined by the point where $V_p = U_{\perp}$ ($s = \pm 50$). (B-D) Cell-substrate adhesions (green springs) oppose myosin-driven retrograde flow (blue arrows) of the actin network (red). When adhesion is strong, or contractile forces are low, the actin network is stationary with respect to the underlying surface ($U_{\perp} = 0$) and actin polymerization drives protrusion of the cell boundary (B). When adhesion is weak or contractile forces are high (C, D), the actin network moves with respect to the underlying surface ($U_{\perp} > 0$). If the rate of polymerization is equal to the rate of retrograde flow ($V_p = U_{\perp}$) then the cell boundary is stationary (C), but if actin polymerization is less than the rate of retrograde flow ($V_p < U_{\perp}$) the cell boundary retracts (D).
doi:10.1371/journal.pbio.1001059.g004

and moves with the actin network. In the reference frame of the cell, the actin network and myosin molecules move towards the rear of the cell with velocity V_{cell} , the net cell migration velocity $v(s)$ at $s=0$, and flows inward from the cell boundary with velocity U_{\perp} .

To determine the effect of adhesion strength on \vec{U} , we simulated myosin distribution and retrograde flow patterns using low, intermediate, and high values for the adhesion drag coefficient, ζ , and input cell shapes and cell velocities measured from the experimental data (Figure 5, see Text S1). Our simulations predict adhesion-dependent feedback between myosin localization and actin network flow. The magnitude of retrograde actin network flow increases as ζ decreases (Figure 5B–5C) and this increase in retrograde flow has consequences for the myosin localization pattern. At intermediate and high ζ , the actin network is nearly stationary with respect to the underlying substrate, so myosin localization in the cell coordinate system is largely controlled by V_{cell} : actin-bound myosin moves towards the cell rear as the cell moves forward at velocity V_{cell} . Cells crawling at high adhesion strength exhibit significantly slower velocities than cells crawling at intermediate adhesion strength (Figure 1C), and our simulations predict that the measured difference in cell speed

should result in different myosin distribution patterns, with increased enrichment of myosin in the cell rear in fast-moving cells crawling at intermediate adhesion strength compared to slow-moving cells crawling at high adhesion strength (Figure 5A, center and right panels; Figure 6E). At low ζ , in addition to moving towards the cell rear in the cell coordinate system with the rate V_{cell} , the actin network moves with respect to the underlying substrate, flowing inward from the cell boundary with the rate U_{\perp} and resulting in the accumulation of actin-bound myosin in a ring around the cell body (Figure 5A, left panel). The myosin distribution pattern, in turn, affects the pattern of retrograde flow, with the highest rates of flow occurring in regions where myosin and its density gradients are enriched (Figure 5A, 5B). Although these retrograde flow and myosin distribution patterns were computed on the average cell shapes measured from experimental data, similar patterns were observed when the same input shape was used for all three cases (Figures S3 and S4), indicating that the observed differences arise from the variations in adhesion strength and are not solely due to differences in the input cell shape.

This sub-model for myosin-mediated retrograde flow makes quantitative predictions about myosin localization and retrograde flow in cells on different adhesion strength surfaces. First, the

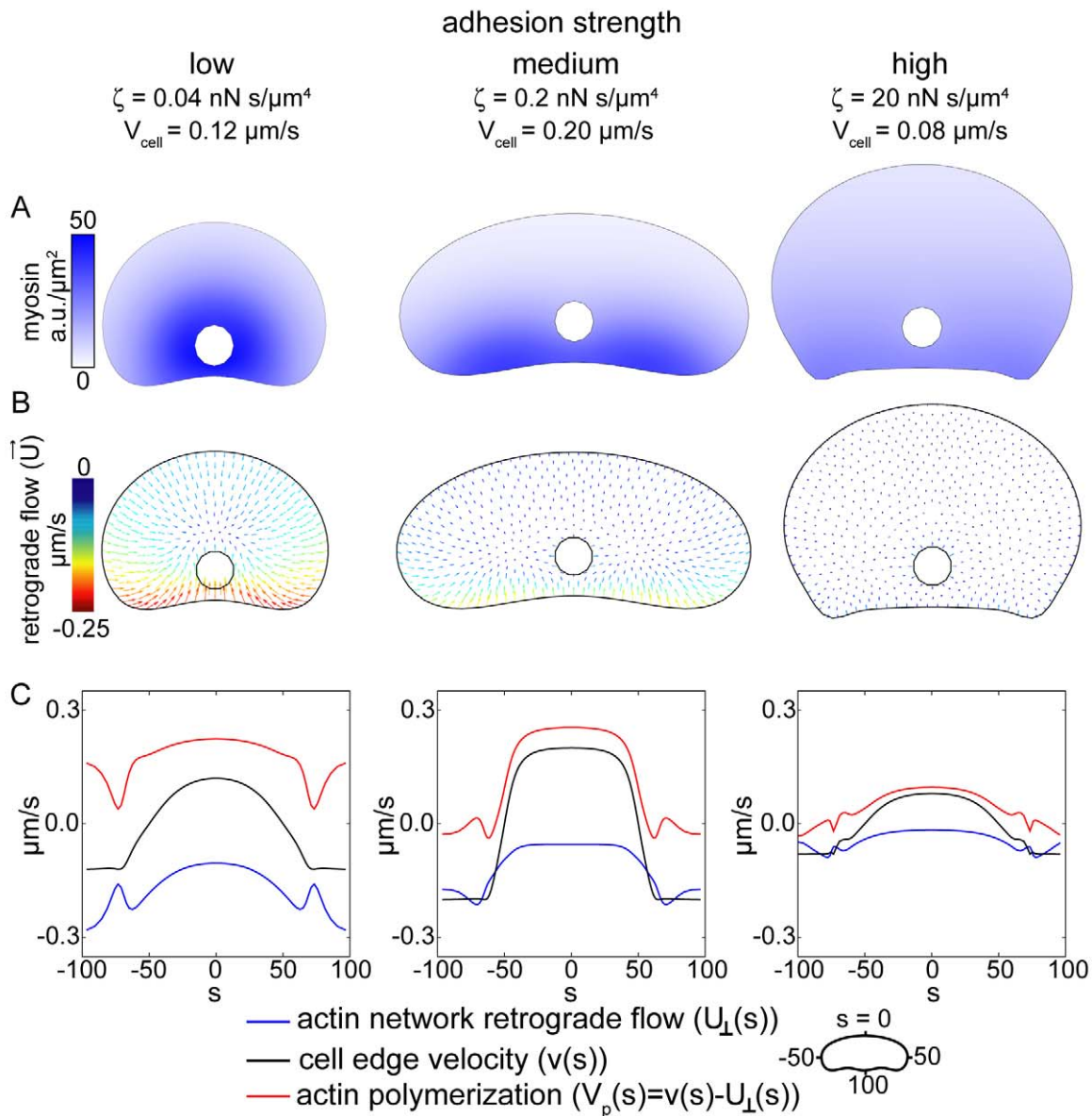


Figure 5. Simulated myosin and retrograde flow patterns. Coupled myosin and flow distributions were computed on the fixed cell shapes for the indicated values for the adhesion drag coefficient, ζ , and cell speed, V_{cell} . Cell shape and V_{cell} were taken from the experimental data. (A) Myosin distributions. (B) Actin network retrograde flow. The direction and magnitude of local actin network movement with respect to the underlying substrate is indicated by color-coded arrows; hot colors correspond to faster flow. (C) Distributions of the computed normal component of the centripetal flow around the boundary (blue), polymerization rate (red) and net protrusion/retraction rate (black). The centripetal flow rates at the boundary were taken from the flow maps shown in (B). The actin polymerization rates are the rates required to maintain the input cell shape, given the simulated retrograde flow patterns. See Text S1 for a detailed description of the model parameters. doi:10.1371/journal.pbio.1001059.g005

model simulations predict specific, adhesion-dependent myosin localization patterns (Figure 5A). To test this, we examined myosin localization patterns in cells plated on low, intermediate, and high adhesion strength surfaces (Figure 6). As predicted, myosin localized to a ring around the cell body in cells crawling at low adhesion strength (Figure 6B, left panel) and localized to the cell rear in cells crawling at intermediate adhesion strength (Figure 6B, center panel). In cells crawling at high adhesion strength, myosin was largely excluded from protruding portions of the leading edge and under the cell body, but was more uniformly distributed in the rest of the cell (Figure 6B, right panel). We compared these experimental myosin distributions to the model simulations by

measuring average myosin densities from the cell front to the cell rear in populations of cells (Figure 6D). We found that myosin accumulated in the cell rear at intermediate adhesion strengths but was more uniformly localized in cells at high adhesion strengths, consistent with the model simulations (Figure 6E). We also found that peak myosin densities were shifted towards the cell interior in cells crawling at low adhesion strengths, consistent with increased inward flow of the actin network and attached myosin molecules at low adhesion strengths.

Second, the model simulations predict that retrograde flow should increase as adhesion strength decreases, with the fastest flow localized to the rear of the cell where myosin is enriched

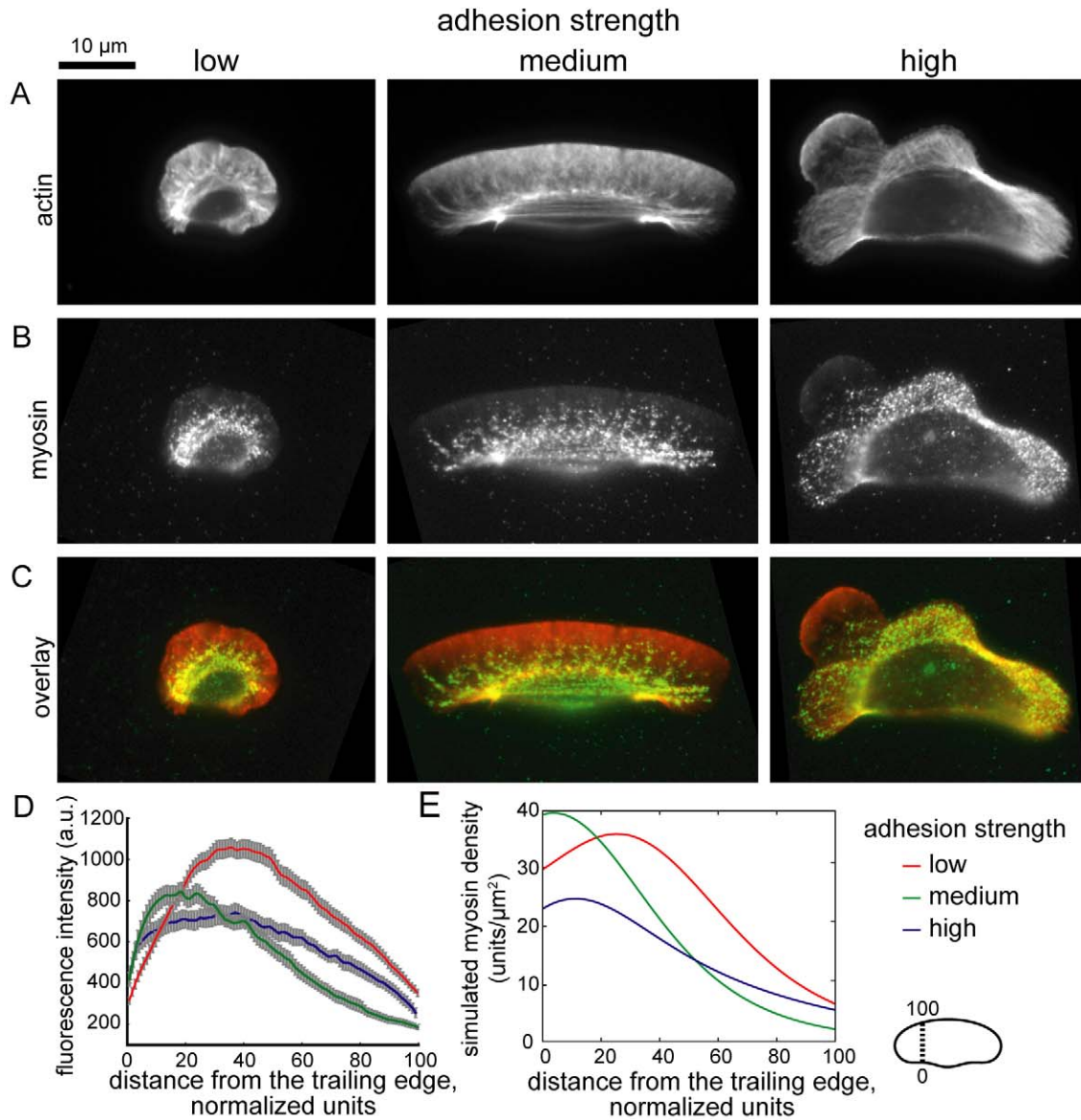


Figure 6. Adhesion strength affects myosin distribution patterns. Images of cells plated on low (left), intermediate (center), and high (right) adhesion strength surfaces and labeled for actin with fluorescent phalloidin (A) and immunolabeled for myosin (B). (C) Overlays of the actin and myosin images; actin is pseudo-colored red, and myosin is pseudo-colored green. (D,E) Experimental (D) and simulated (E) myosin distributions, measured from the cell rear (point 0) to the cell front (point 100) on either side of the cell body, for cells plated on low ($n=31$ cells), intermediate ($n=22$ cells), or high ($n=20$ cells) adhesion strength surfaces. Error bars indicate standard error of the mean.
doi:10.1371/journal.pbio.1001059.g006

(Figure 5). To test this, we measured actin network dynamics by fluorescence speckle microscopy (Figure 7). We measured retrograde flow of the actin network by measuring flow relative to the underlying substrate (the lab frame of reference, Figure 7C) as well as actin polymerization rates by measuring flow relative to the cell perimeter (the cell frame of reference, Figure 7B). As predicted, retrograde flow of actin increased as adhesion strength decreased (Figure 7C, 7D). The rate of actin polymerization also increased with decreasing adhesion strength (Figure 7B and 7D), suggesting that in addition to affecting retrograde flow, adhesion strength also affects actin network growth rates. Moreover, the distribution of actin polymerization and retrograde flow rates around the cell boundary varied with adhesion strength (Figure 7D). At low adhesion strengths, the magnitude of

retrograde flow was graded (U_{\perp} increased from $0.11 \pm 0.06 \mu\text{m/s}$ at $s=0$ to $0.25 \pm 0.10 \mu\text{m/s}$ at $s = \pm 50$) and the magnitude of actin polymerization along the leading edge was constant ($V_p = 0.25 \pm 0.08 \mu\text{m/s}$ at $s=0$ and at $s = \pm 50$, $n=35$ cells). At intermediate and high adhesion strengths, in contrast, the magnitude of retrograde flow was nearly constant along the leading edge ($U_{\perp} = 0.03 \pm 0.02 \mu\text{m/s}$ at $s=0$ and $0.06 \pm 0.04 \mu\text{m/s}$ at intermediate adhesion strength; $U_{\perp} = 0.04 \pm 0.03 \mu\text{m/s}$ at $s=0$ and $0.06 \pm 0.06 \mu\text{m/s}$ at $s = \pm 50$ at high adhesion strength) and the rate of actin polymerization decreased in a dramatic, step-like fashion ($V_p = 0.22 \pm 0.05 \mu\text{m/s}$ at $s=0$ and $0.06 \pm 0.06 \mu\text{m/s}$ at $s = \pm 50$ at intermediate adhesion strength, $n=46$ cells; $V_p = 0.13 \pm 0.09 \mu\text{m/s}$ at $s=0$ and $0.06 \pm 0.06 \mu\text{m/s}$ at $s = \pm 50$ at high adhesion strength, $n=23$ cells). These

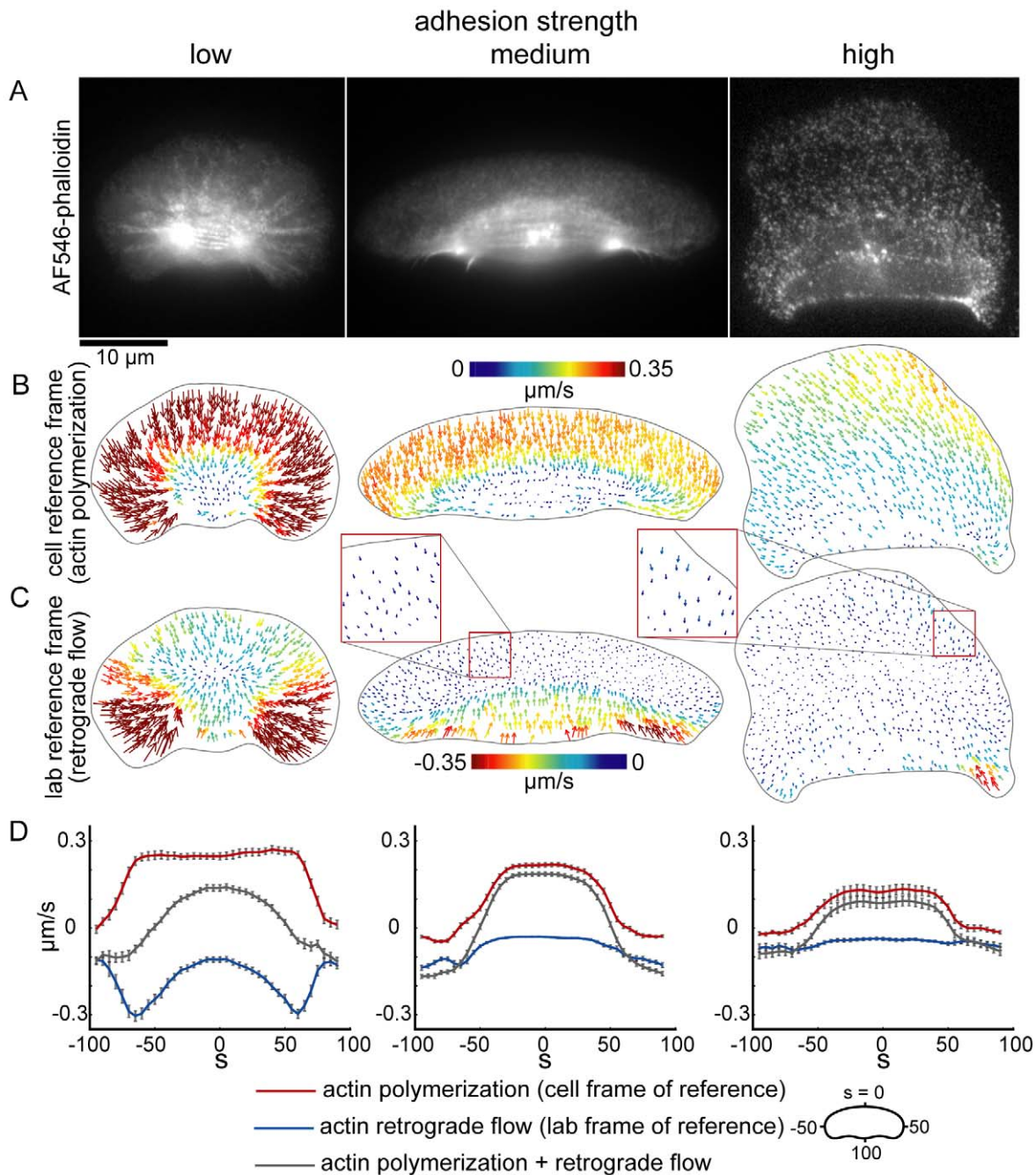


Figure 7. Actin polymerization and retrograde flow rates decrease as adhesion strength increases. (A) Images of keratocytes labeled with a low concentration of AlexaFluor546-phalloidin, plated on low (left), intermediate (center), and high (right) adhesion strength surfaces. (B,C) Actin network flow maps in the cell frame of reference (B), corresponding to actin polymerization, and in the lab frame of reference (C), corresponding to retrograde flow of the actin network, are shown for the cells shown in (A). (D) Average actin polymerization rates (red lines), actin retrograde flow rates (blue lines) measured in populations of cells plated on low ($n=36$ cells), intermediate ($n=46$ cells), and high ($n=25$ cells) adhesion strength surfaces are plotted for each point around the cell perimeter. The gray lines are the effective cell boundary expansion/retraction rates calculated by adding the measured actin polymerization and retrograde flow rates. Error bars indicate standard error of the mean. doi:10.1371/journal.pbio.1001059.g007

measured actin polymerization and retrograde flow distributions are consistent with the simulated distributions (compare Figures 5C and 7D) and suggest that as adhesion strength increases, the mechanism for cell shape and speed determination switches from dependence on retrograde actin network flow to dependence on actin polymerization. Specifically, these results

suggest that cells at low adhesion strength are rounder and slower than cells at intermediate adhesion strength, despite increased actin polymerization, because of increased retrograde flow at the cell front and sides, whereas cells on high adhesion strength are slower and rounder because of reduced actin polymerization rates.

Finally, the model predicts that tuning the level of myosin activity with respect to adhesion strength should affect actin retrograde flow rates, with fast retrograde flow occurring when myosin activity is high relative to adhesion strength (Figure S5). To test this prediction experimentally, we treated cells crawling at low, intermediate, and high adhesion strengths with either blebbistatin, a myosin II inhibitor [39], or calyculin A, a phosphatase inhibitor that activates myosin contraction [40]. Although calyculin A has multiple targets, its effects on cell shape and speed in keratocytes appear to be dominated by its effects on myosin II activity (see Figure S6 and Text S2). As predicted, we found that myosin inhibition reduced retrograde flow and activation of myosin contraction increased retrograde flow (Figure 8B, Figure S7), consistent with model simulations (Figure S5). Actin polymerization rates also increased with increasing myosin activity (Figure 8A, Figure S7), indicating that the balance between adhesion strength and myosin contraction (rather than the absolute magnitude of either) determines the rate of actin network growth, as well as the rate of retrograde flow. In addition, we found that myosin-dependent changes in actin polymerization and retrograde flow rates were associated with changes in cell shape and velocity (Figure 8C–8E). Area and aspect ratio increased in cells treated with blebbistatin, particularly in cells at low adhesion strength, and decreased in cells treated with calyculin A (Figure 8D–8E). Cell velocity, conversely, increased in cells treated with calyculin A, at all adhesion strengths, suggesting that increased actin polymerization more than compensates for increased retrograde flow when myosin activity is enhanced.

Establishment of Adhesion and Actin Network Density Distributions

The sub-model for myosin-driven retrograde flow detailed above is consistent with experimental measurements of retrograde flow and cell shape, but by itself does not address the observed adhesion- and myosin-dependent actin polymerization distributions (Figures 7B and 8A). Previously published measurements of keratocyte shapes and actin network distributions are consistent with a model in which the rate of actin polymerization along the cell perimeter, $V_p(s)$, emerges from mechanical feedback between the actin network and the cell membrane [29]. Specifically, $V_p(s)$ is thought to depend on the organization and density of actin filaments, the concentration of free actin monomers, and membrane tension, which imposes a force on the actin network, slowing filament growth [29]: $V_p(s) = V_0 \left(1 - \left(\frac{T}{f_{\text{stall}} D(s)} \right)^w \right)$, where V_0 is the free actin polymerization rate proportional to the actin monomer concentration, T is membrane tension, D is the local density of actin filaments, f_{stall} is the force at which polymerization stalls, and $w \sim 8$ is the parameter characterizing the force-velocity relationship for actin polymerization. We assume that within individual cells actin monomer concentration and membrane tension are globally constant—actin monomers rapidly diffuse throughout the cell, and local perturbations in membrane tension rapidly equilibrate—but actin filament densities along the leading edge have been shown to be graded in keratocytes, with enrichment of branched filaments at the center of the leading edge and enrichment of bundled filaments at the trailing edge [29,30]. Large adhesion complexes localize to the trailing edge in keratocytes [30,41,42] and large, stable adhesions are associated with reduced protrusion in Chinese hamster ovary (CHO) cells [43]. Myosin also localizes predominantly to the cell rear in keratocytes (Figure 6) and is thought to promote actin depolymerization [26]. Therefore, we propose that antagonism between adhesion complexes and the dendritically branched actin network

and myosin-mediated actin depolymerization determine the actin filament distribution along the cell perimeter, $D(s)$ (see Text S1).

We simulated adhesion and actin distributions and the rate of actin polymerization along the cell boundary, $V_p(s)$, based on the retrograde flow maps and myosin distributions simulated in Figure 5. To model the adhesion distribution (which we model as a continuous distribution, rather than as discrete adhesion complexes), we assume that adhesions assemble and disassemble with constant rates throughout the cell. Adhesions are malleable structures that are partially dragged along the surface due to coupling with the actin network [11]; thus, in the cell coordinate system, their localization depends on the speed with which the cell moves over them, and the rate of retrograde flow of the actin network within the cell. Simulations of this model (see Text S1 for a discussion of model parameters) show that at low adhesion strength, adhesions are swept inward due to high rates of retrograde flow (Figure 9A, 9C, left), and therefore do not inhibit polymerization of the branched actin network, resulting in uniform distributions of actin filaments around the cell perimeter (Figure 9B–9C, left). In contrast, at intermediate and high adhesion strengths, reduced rates of retrograde flow allow adhesion complexes to accumulate in the cell rear (Figure 9A, 9C, center and right) and inhibit actin polymerization, resulting in enrichment of actin filaments at the center of the leading edge (Figure 9B, 9C, center and right). We examined actin network organization and adhesion distribution (as measured by vinculin localization) in cells plated on low, intermediate, and high adhesion strength surfaces (Figure 10), and found that adhesion complexes were most enriched in regions of the cell predicted to have the highest adhesion densities (compare the simulated distributions in Figure 9A and 9C with the experimental data shown in Figure 10A and 10C). Small, punctate adhesions localized to a ring around the cell body in cells plated at low adhesion strengths (Figure 10B, left panel), whereas larger, elongated adhesions localized to the trailing edge in cells at intermediate adhesion strength (Figure 10B, center panel). At high adhesion strength, large adhesions were biased towards the cell rear, but also localized to stalled portions of the leading edge (Figure 10B, right panel). In all cases, elongated adhesions were spatially correlated with a reduction in dendritically branched F-actin and an increase in bundled actin filaments, resulting in uniform actin distributions in cells plated on low adhesion strength surfaces, and in peaked distributions in cells on intermediate and high adhesion strength surfaces (Figure 10C, compare to Figure 9C). Overall, these results are consistent with the hypothesis that large adhesions antagonize the assembly of a dendritically branched actin network.

The simulated and experimentally observed distributions of mature adhesions described above are spatially heterogeneous (Figures 9 and 10), which is seemingly at odds with our initial assumption that the adhesion drag coefficient ζ is spatially constant. However, the relationship between adhesion size and age and adhesion strength is not well understood: depending on the cell type, traction force measurements suggest that adhesion strength either increases [22], decreases [44], or does not correlate [10] with adhesion size. Therefore, we simulated actin network flow patterns and myosin, adhesion, and actin distributions for three different cases. In the cases where ζ is spatially constant (Figures 5 and 9) or decreases with adhesion density (Figure S8; see Text S1), the simulated patterns matched the experimentally observed patterns. However, in the case where ζ increases with adhesion density, the simulated patterns of retrograde actin flow did not match the experimentally observed patterns (Figure S9). Specifically, the rate of retrograde flow was nearly constant around

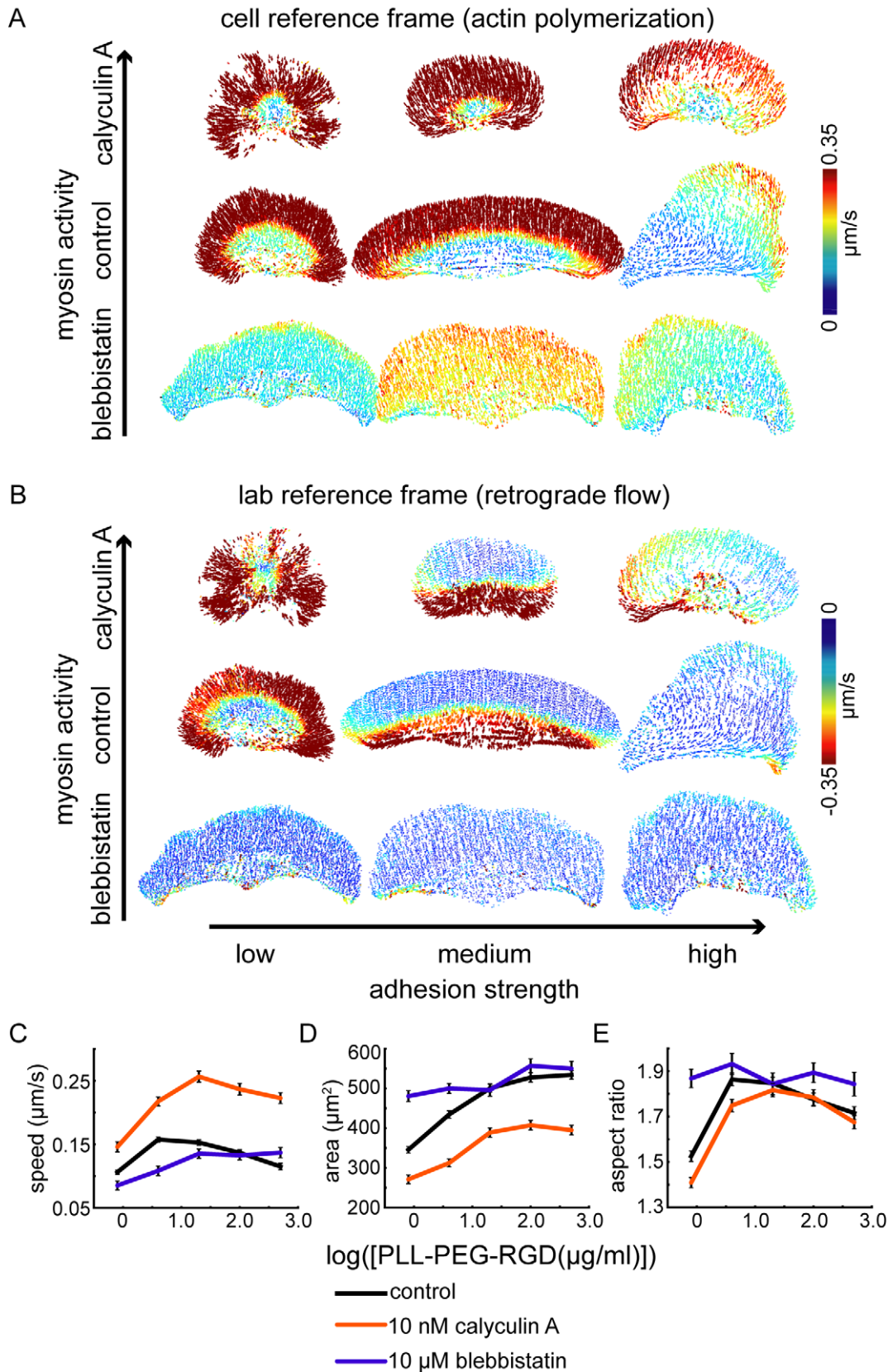


Figure 8. The balance between adhesion strength and myosin activity determines actin polymerization and retrograde flow rates and cell speed and shape. (A,B) Representative flow maps in the cell frame of reference, corresponding to actin polymerization (A), and lab frame of reference, corresponding to retrograde flow (B), are shown for cells crawling at low (left), intermediate (center), and high (right) adhesion strength

and treated with either 10 nM calyculin A (top), 10 μ M blebbistatin (bottom), or no drug (middle). Average cell speed (C), area (D), and aspect ratio (E) for populations of cells treated with blebbistatin (blue lines) or calyculin A (orange lines) are shown for cells plated on surfaces coated with the indicated PLL-PEG-RGD concentrations. The data for control cells, shown in Figure 1, is re-plotted here for comparison (black lines). Error bars indicate standard error of the mean.

doi:10.1371/journal.pbio.1001059.g008

the cell perimeter at intermediate values for ζ rather than increasing in the cell rear as observed experimentally (Figure S9C, S9D, Figure 7C, 7D). Thus, our findings are most consistent with a pattern of adhesion strength that is nearly constant or decreasing from the front to the rear of migrating cells. Indeed, this latter pattern is most consistent with the idea that cells must release adhesions in the rear in order to move forward, and is also well-supported by recent experiments that measured the spatial pattern of traction forces exerted on the underlying substrate by migrating keratocytes [9].

Emergence of Cell Shape from the Interaction of Mechanical Forces

Our proposed model nicely recapitulates experimental actin flow patterns, as well as myosin, adhesion, and actin distributions, for low, intermediate, and high adhesion strengths. Finally, to model the effect of adhesion strength on cell shape, we performed dynamic modeling of actin polymerization, retrograde flow, and cell shape using an iterative procedure (see Text S1, Movie S6). Starting with a round input shape (Figure 11A), we solved for \bar{U} and $V_p(s)$ using a low adhesion drag coefficient, $\zeta = 0.04 \text{ nNs}/2\mu\text{m}^4$ (see Text S1). We allowed the input shape to deform in response to the simulated expansion and retraction rates, and the simulation was repeated until the shape converged to a stable shape and flow pattern. The simulations converged to a shape with low aspect ratio and fast retrograde flow at the cell sides and rear (Figure 11B), consistent with the experimental data (Figure 1E, Figure 7C, left panel). Then, we increased the adhesion drag coefficient to an intermediate value, $\zeta = 0.02 \text{ nNs}/2\mu\text{m}^4$, and repeated the simulations again until the shape converged to a new stable shape. With the intermediate adhesion drag coefficient, the simulations converged to a shape with higher aspect ratio and lower retrograde flow rates (Figure 11C), also consistent with the experimental data (Figure 1E, Figure 7C, center panel). Altogether, these results demonstrate that a self-consistent, self-organizing model in which cell shape emerges from interactions among the actin network, myosin, adhesions, and the cell membrane recapitulates the observed adhesion-dependent changes in steady-state cell shape.

Discussion

We have presented a model in which overall cell shape depends on mechanical feedback among the actin network, myosin, adhesions, and the cell membrane. In this model, extension of the cell perimeter, and thus cell shape, is determined by the vectorial sum of retrograde flow of the actin network and actin network growth. Specifically, the cell front is defined by the region where polymerization rates are greater than retrograde flow rates, the cell rear is defined by the region where retrograde flow rates are greater than actin polymerization rates, and the relative positions of the cell corners are defined by the points where the two rates are perfectly balanced (Figure 4). The rate of retrograde flow at each point around the cell perimeter depends on the local balance between adhesion and myosin-mediated contraction of the actin network. The spatial pattern of retrograde flow rates is determined by an asymmetric distribution of myosin molecules: myosin associates with the actin network and accumulates in the

rear of the cell as the cell moves forward, resulting in increased myosin contraction and retrograde flow in the cell rear. The rate of actin polymerization at each point around the cell perimeter depends on the density of branched actin filaments. Adhesions, like myosin, accumulate in the cell rear as the cell moves forward, and we propose that myosin- and adhesion-mediated reduction of branched actin density in the cell rear effectively biases fast actin polymerization towards the cell front.

Simulations of this model predict an adhesion-dependent switch between mechanisms that determine cell shape. At intermediate and high adhesion strengths, myosin and adhesions localized to the trailing edge reduce the density of the branched actin network, thereby establishing a graded distribution of pushing actin filaments (Figures 5A and 9). As the density of actin filaments decreases towards the cell sides, membrane tension stalls actin polymerization [29]. Retrograde flow of the actin network is slow and fairly constant from the cell front to the cell sides (Figure 5B, 5C), so reduced actin polymerization, rather than increased retrograde flow, sets the relative positions of the cell corners. At low adhesion strength, in contrast, myosin and adhesions are swept to the cell interior by retrograde flow of the actin network (Figure 5A and 9A), preventing myosin- and adhesion-mediated reduction of F-actin density and resulting in a uniform distribution of F-actin and actin polymerization rates from the cell front to the cell sides (Figure 5C and 9C). Retrograde flow, on the other hand, is graded, increasing dramatically from the cell front to the cell side (Figure 5B, 5C). Thus, at low adhesion strength, increased retrograde flow, rather than reduced actin polymerization, sets the relative positions of the cell corners. We have presented experimental evidence that is consistent with the predictions of this model: as adhesion strength decreased, retrograde flow of the actin network increased (Figure 7C, 7D), myosin and adhesions switched from localization to the trailing edge to localization to a ring around the cell body (Figures 6 and 10B, 10C), and the actin filament density along the leading edge became less graded (Figure 10A, 10C). In addition, we found that inhibiting or activating myosin contraction either decreased or increased retrograde flow (Figures 8, S5), as predicted by model simulations (Figure S4). Finally, numerical simulations correctly recapitulated the effect of adhesion strength: as predicted (Figure 11), keratocytes were fan-shaped at intermediate adhesion strength and round at low adhesion strength (Figure 1E). These results are consistent with our model in which the self-organization of the dynamic actin network, myosin, and adhesions determines motile cell shape.

Integrin-based adhesions are both mechanical structures that resist myosin-driven actin network flow and organizing centers that localize biochemical signals that contribute to the organization of the actin network [13,45]. The mechanical model for cell shape determination described here does not explicitly incorporate biochemical signaling pathways. However, we argue that the myriad effects of integrin signaling are relevant for cell shape determination only insofar as they affect the localization and activity of molecules that contribute to mechanical feedback among the actin network, adhesions, myosin, and the cell membrane. For example, integrin signaling is thought to promote both Rac and RhoA GTPase activity, with nascent adhesions promoting Rac activity [14] and mature adhesions promoting

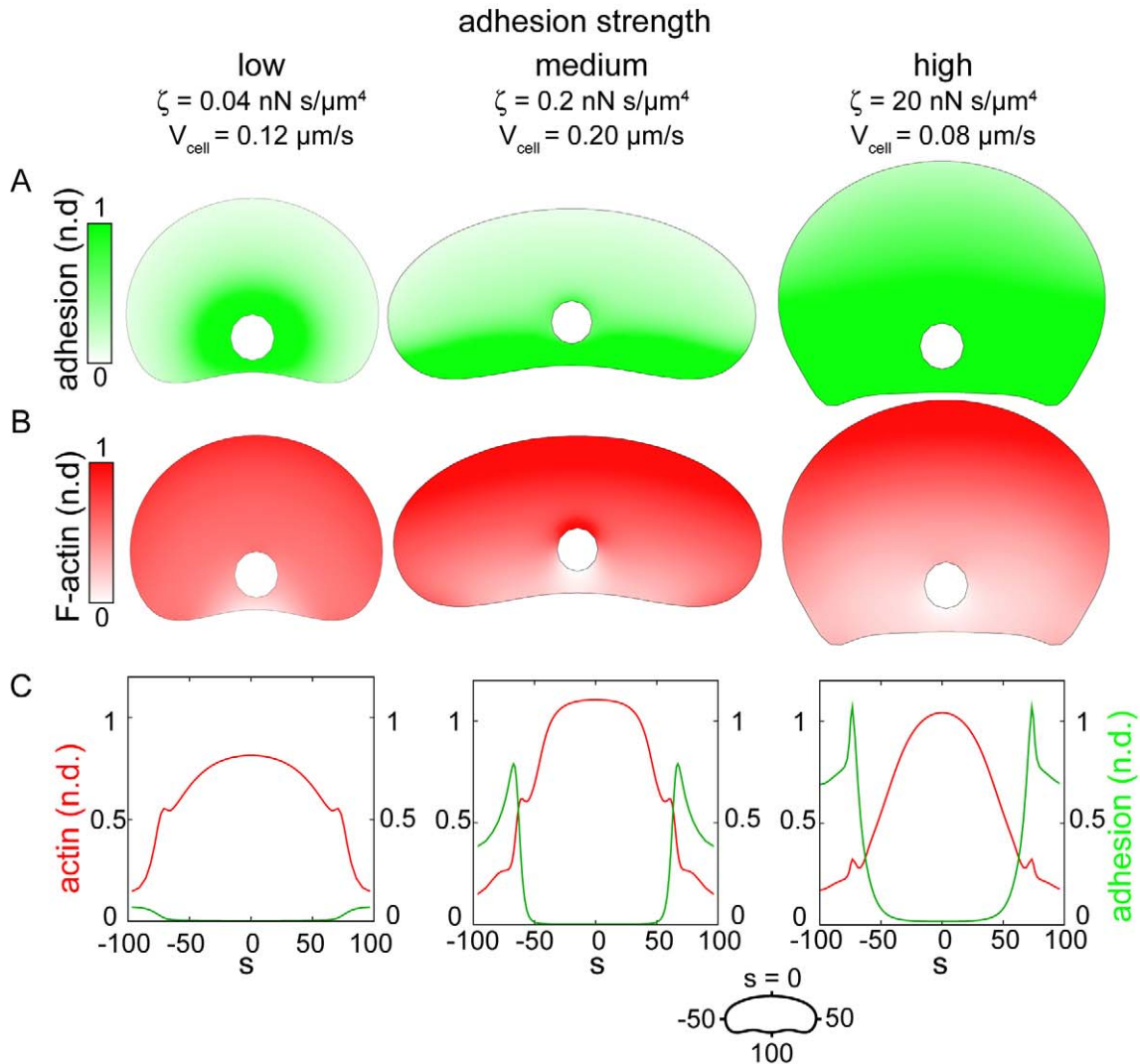


Figure 9. Simulated adhesion and actin filament distribution patterns. Coupled adhesions and actin distributions were computed from the actin network flow patterns shown in Figure 5 for low (left), medium (center) and high (right) adhesion strengths. (A) Simulated adhesion distributions. (B) Simulated F-actin distributions. (C) Distributions of the computed adhesion (green) and F-actin (red) densities around the cell perimeter. Units are non-dimensionalized (n.d.). See Text S1 for simulation parameters.
doi:10.1371/journal.pbio.1001059.g009

RhoA activity [19]. Increased Rac activity promotes protrusion by activating Arp2/3 [15,16], increasing the number of barbed ends. Therefore, the effect of increased Rac activity can be reduced to the mechanical consequences of increasing the density of actin filaments at the cell boundary, which is described in our mechanical sub-model for actin polymerization. One of the consequences of increased RhoA activity, on the other hand, is activation of myosin light chain kinase and up-regulation of myosin activity [21], which can be reduced to the mechanical consequences of increasing contractile forces, which is described in our mechanical model for actin network retrograde flow. Recent efforts to model individual mechanical process important for cell migration have included some aspects of integrin signaling, including a recent kinetic model for actin-integrin “clutch” dynamics [46]. Although our model does not currently incorporate integrin signaling, future efforts could be made to include the specific contributions of signaling pathways to the general mechanical mechanisms described here.

In our model for actin network polymerization, antagonism between adhesions and the branched actin network, along with myosin-mediated actin depolymerization and cooperative actin network branching, establishes a graded distribution of F-actin along the leading edge. This graded actin network distribution has been measured previously [29,30]; here we show that decreased actin filament densities spatially correlate with large, elongated adhesions at intermediate and high adhesion strengths. At low adhesion strength, keratocytes exhibit only small, punctate adhesions and have relatively uniform F-actin distributions along the leading edge. These results are consistent with the idea that mature adhesions inhibit assembly of the branched actin network, but the mechanism for this antagonism between mature adhesions and the branched actin network is unknown. Mature adhesions have been shown to promote formation and polymerization of actin bundles [47–49] and this adhesion-dependent filament bundling may be sufficient to switch the actin network to a bundled architecture incompatible with lamellipodia-based pro-

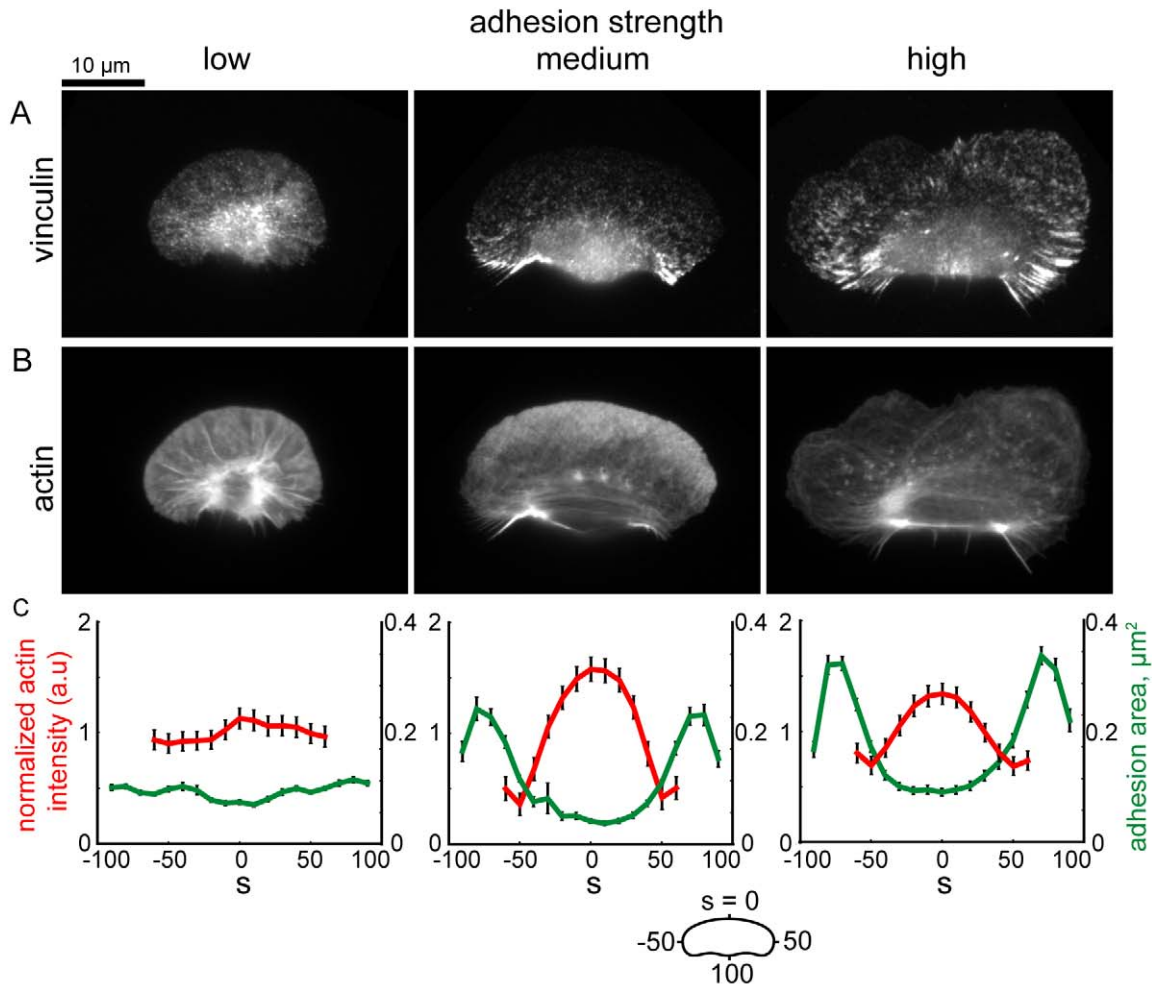


Figure 10. Large, elongated adhesions spatially correlate with a reduction in branched actin network density. (A,B) Images of cells immunolabeled for vinculin (A) and labeled for actin with fluorescent phalloidin (B). (C) Average actin intensity (red line) and adhesion area (green line) are plotted for points along the cell perimeter for cells plated on low ($n = 176$ cells), medium ($n = 136$ cells), and high ($n = 179$ cells) adhesion strength surfaces. Actin intensities are normalized such that the mean intensity for each cell is equal to 1. Error bars indicate standard error of the mean.

doi:10.1371/journal.pbio.1001059.g010

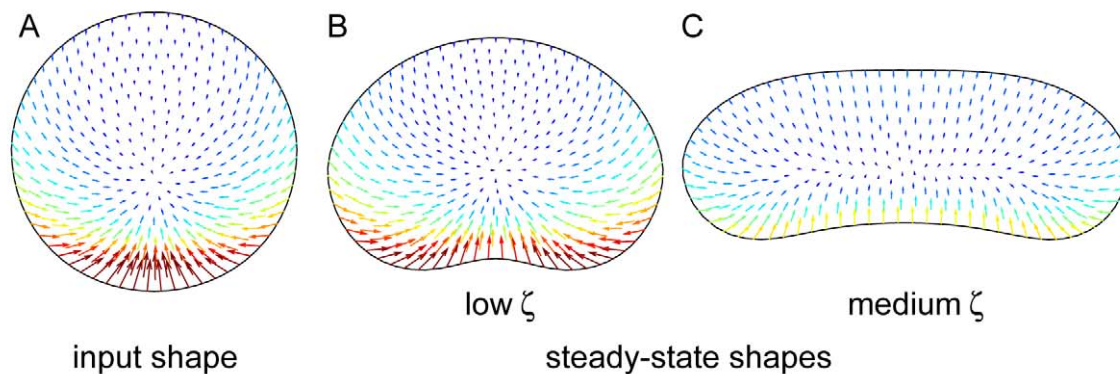


Figure 11. Dynamical simulations of cell shape for different adhesion drag coefficients recapitulate experimentally observed differences in cell shape. Cell shape and actin network flow were simulated using an iteration procedure (see Text S1). Cell shape and actin flow at the cell boundary are shown for the input shape (A), the stable shape that evolved at low adhesion strength (B; $\zeta = 0.04$ nNs/ μm^4), and the stable shape that evolved at intermediate adhesion strength (C; $\zeta = 0.2$ nNs/ μm^4).

doi:10.1371/journal.pbio.1001059.g011

trusion. In addition, nascent adhesions are thought to trigger a positive feedback loop that promotes actin polymerization and leading edge protrusion downstream from Rac GTPase [14], and adhesion maturation may antagonize actin polymerization by disrupting this feedback loop [43].

Our model recapitulates the observed adhesion-dependent changes in retrograde flow patterns and myosin, adhesion, and F-actin distributions, but it does not directly account for adhesion- and myosin-dependent changes in actin polymerization rates. We have found that actin polymerization rates increase with decreasing adhesion (Figure 7) and decrease with decreasing myosin activity (Figure 8, Figure S5). Actin polymerization rates depend on the concentration of free actin monomers and the force per actin filament imposed by the cell membrane [50,51]. Membrane tension may increase as the strength of adhesion increases relative to myosin contraction: when adhesion strength is high and myosin activity is low, cell area increases, potentially stretching the cell membrane and increasing membrane tension. However, measurements of membrane tension in keratocytes at low, intermediate, and high adhesion strengths have shown that changes in membrane tension alone are not sufficient to account for the changes in actin polymerization rates (E. Barnhart, A. Leibler, and K. Keren; unpublished data). The balance between adhesion and myosin strength may also affect the concentration of actin monomers: adhesions have been shown to promote polymerization of actin bundles [47] and myosin contraction has been shown to promote actin depolymerization [26]. Therefore, we propose that the balance between myosin contraction and adhesion strength influences the concentration of free actin monomers, with the monomer concentration increasing as adhesion size decreases or myosin activity increases, resulting in a global increase in the actin polymerization rate.

Our results indicate that increased actin polymerization can compensate for increased actin retrograde flow in keratocytes. We found that cell speed increased in cells treated with calyculin A, a phosphatase inhibitor that promotes myosin contraction [40], at all adhesion strengths (Figure 8C). In these cells, increased actin polymerization more than compensated for increased retrograde flow of the actin network at the front of the cell (Figure S5). Cell speed did not change in some individual cells as they crawled from regions of low to intermediate adhesion strength (Figure 3C, 3F), consistent with the idea that increased actin polymerization compensates for increased retrograde flow at low adhesion strengths. Similarly, non-adhesive dendritic cells have been shown to migrate at speeds comparable to those of adhesive dendritic cells despite increased retrograde flow, suggesting that increased actin polymerization compensates for increased retrograde flow to maintain constant cell speed [52]. Together, these results are consistent with the idea that cell speed is determined by the sum of actin polymerization and retrograde flow rates in simple-shaped, fast-moving cells like keratocytes and dendritic cells. In slow-moving cells such as PtK1 cells, however, the relationship between actin polymerization and retrograde flow rates and cell speed is more complicated [3]: although instantaneous protrusion and retrograde flow rates in migrating PtK1 cells are comparable to those measured in keratocytes, with protrusion rates as fast as $\sim 0.3 \mu\text{m/s}$ and retrograde flow rates on the order of $0.01 \mu\text{m/s}$, cell speed is an order of magnitude lower in PtK1 cells ($\sim 0.01 \mu\text{m/s}$ in PtK1 cells, compared to $0.1 \mu\text{m/s}$ in keratocytes). The balance between adhesion strength and myosin contraction has been shown to control cell speed in these cells [3]. Unlike keratocytes, PtK1 cells do not exhibit steady-state shapes and speeds, and thus more complicated adhesion- and myosin-

dependent mechanisms are likely to control cell speed in these cells.

Although fish keratocytes are renowned for their ability to maintain steady-state shapes and velocities over hundreds of microns of migration [1,27,29,30,33], they have also been shown previously to exhibit non-steady-state dynamic behaviors, including spontaneous symmetry breaking and motility initiation [53] and oscillatory retraction of the trailing edge [54]. Here we have found that traveling waves of protrusion emerge in keratocytes as adhesion strength increases (Figures 2 and 3). In these cells, similar to PtK1 cells, overall cell speed is significantly slower than protrusion rates along short sections of the leading edge (cell speed = $0.06 \mu\text{m/s}$, compared to maximum protrusion velocity = $\sim 0.2 \mu\text{m/s}$ for the cell shown in Figure 2). The steady-state model described here cannot account for these protrusion waves, but regular oscillations in protrusion have been previously observed in other cell types [55–62]. Proposed mechanisms for these protrusion oscillations include mechanical feedback between adhesion formation at the leading edge and myosin contraction [58] and a mechanism in which Rho GTPase activation at the leading edge promotes initial protrusion [60]. We favor a third mechanism, in which mature focal adhesions titrate actin polymerization activators away from the leading edge, resulting in the emergence of waves of protrusion. A detailed model for oscillation of the leading edge in keratocytes crawling at high adhesion strength will be published elsewhere.

Migrating cells take many shapes and move at different velocities, ranging from triangular-shaped, slow-moving fibroblasts to amoeboid-shaped, fast-moving neutrophils and fan-shaped, fast-moving fish keratocytes [28]. These various cell shapes and migration speeds are the manifestation of the underlying dynamics and mechanics of the cytoskeleton. Top-down modeling of cell shape has demonstrated that quantitative changes in “control parameters” such as adhesion strength are sufficient to switch cells between different shapes [63]. Here, we have presented a bottom-up model for keratocyte shape determination that emerges from known biochemical and mechanical interactions among the cellular components involved in force generation for cell motility. We have found that changes in adhesion strength and myosin activity are sufficient to switch keratocytes between migration regimes, including one on high adhesion strength surfaces in which the typically fan-shaped, fast-moving keratocytes begin to resemble slow-moving fibroblasts. Thus, quantitative, rather than qualitative, differences in control parameters are likely to be sufficient to explain the different cell shapes and behaviors observed for different cell types.

Materials and Methods

Keratocyte Culture and Labeling

Keratocytes were cultured from the scales of the Central American cichlid *Hypsophrys nicaraguensis* as described [30]. Briefly, scales were sandwiched between two acid-washed coverslips and cultured in Leibovitz's Media (L-15) supplemented with 14.2 mM HEPES pH 7.4, 10% FBS, and 1% antibiotic-antimycotic at room temperature for 12–24 hours. Keratocytes were replated by trypsinization: cells were washed briefly with PBS and then treated with 0.1% trypsin and 1 mM EDTA in PBS for 5 minutes. The trypsin was quenched with a ten-fold excess of culture media and the cells were transferred directly to PLL-PEG-RGD coated surfaces and allowed to recover for one hour. Pharmacological agents including blebbistatin and calyculin A were applied to cells 10–30 minutes prior to imaging.

AlexaFluor546 phalloidin (AF546-phalloidin, Invitrogen) was used to label F-actin for fluorescent speckle microscopy (FSM). 2 μ M AF546-phalloidin was mixed with 7 μ M dATP, 7 μ M GTP, and 5 μ M CTP for 15 minutes at room temperature to prevent phalloidin aggregation. The phalloidin mixture was introduced into keratocytes using a small volume electroporator for adherent cells with three pulses at 150 V.

Synthesis of Surface Coating Materials

PLL-PEG, PLL-PEG-RGD, and PLL-PEG-FITC copolymers were synthesized as described [35,64]. Functionalized PEGs—hetero-bifunctional 3.4 kDa PEG with vinyl-sulfone (VS) and N-hydroysuccinimide (NHS) termini (VS-PEG-NHS), monofunctional 2 kDa mPEG-NHS, and 5 kDa FITC-PEG-NHS—and 15–30 kDa PLL were dissolved separately in HEPES pH 8.4, mixed at a ratio of one PEG chain per 3.5 lysine residues and final PEG concentration of 24 mM, and then stirred for 3 hours at room temperature. For PLL-PEG and PLL-PEG-FITC, all PEG chains were mPEG-NHS or FITC-PEG-NHS, respectively. For PLL-PEG-RGD, 50% of the PEG chains were VS-terminated and, after the 3 hour incubation with PLL, a 4-fold molar excess of RGD peptides (N-acetyl-GCRGYGRGDSPG-amide) was added to the reaction, which was then stirred for an additional 24 hours at room temperature before quenching with 50 mM beta-mercaptoethanol. The samples were dialyzed against ddH₂O, lyophilized, and stored at -20°C . The PLL-PEG-FITC reaction was kept in the dark throughout the synthesis.

Surface Preparation

To generate surfaces with a range of RGD peptide densities, PLL-PEG and PLL-PEG-RGD were dissolved in PBS and mixed at various ratios, with a final total concentration of 0.5 mg/ml. Glass coverslips were washed with acetone and isopropanol, coated with PLL-PEG/PLL-PEG-RGD for 20 minutes at room temperature with slow rocking, and thoroughly rinsed with ddH₂O. The surfaces were either used immediately or stored for up to 24 hours at $+4^{\circ}\text{C}$.

Surfaces patterned with 50 μ m stripes were generated by microcontact printing [65]. To generate stamp masters, silicon wafers were spin-coated with photoresist (SPR 220-7.0) for 1 minute at 1700 rpm, resulting in a resist thickness of 10 μ m. The resist was baked for 90 seconds at 115 C, exposed through a photomask for 45 seconds, and developed for 5 minutes in MF319 developer. Poly(dimethyl)siloxide (PDMS, Sylgard 184) stamps were prepared by mixing the resin and curing agent at a 10:1 v/v ratio. The elastomer was poured over the stamp master and degassed before baking at 80°C for 2 hours. The stamps were cleaned with acetone and isopropanol and incubated with 0.5 mg/ml PLL-PEG/PLL-PEG-RGD, plus 1% PLL-PEG-FITC, for 40 minutes in the dark. The stamps were then dried with clean air and placed on acetone-cleaned glass coverslips for approximately 15 seconds. The surfaces were washed thoroughly with ddH₂O, backfilled with 0.5 mg/ml PLL-PEG/PLL-PEG-RGD for 20 minutes, and washed again with ddH₂O. In all cases, the ratio of PLL-PEG-RGD to PLL-PEG was greater in the stamped solution than in the backfill.

Immunofluorescence

Indirect immunofluorescence was performed using monoclonal mouse anti-vinculin (hVIN-1, ab11194, Abcam, Cambridge MA) and polyclonal rabbit anti-myosin antibodies (ab2480, Abcam, Cambridge MA). For vinculin staining, cells were fixed at room temperature with 4% formaldehyde in 0.32 M sucrose in PBS for 15 minutes, permeabilized with 0.5% Triton X-100 for 10

minutes, and blocked with PBS-BT (3% BSA, 0.1% Triton X-100, and 0.02% sodium azide in PBS) for 30 minutes prior to incubation with primary antibody diluted in PBS-BT. F-actin was labeled with fluorescently conjugated phalloidin. For myosin staining, cells were extracted with 4% PEG and 1% Triton X-100 in cytoskeleton stabilizing buffer (50 mM imidazole, 50 mM KCl, 0.5 mM MgCl₂, 1 mM EDTA, 1 mM EGTA, and 0.5 M TMR-phalloidin) for 5 minutes as described [26], rinsed three times with PBS, blocked with PBS-BT for 5 minutes, and then incubated with primary antibody diluted in PBT-BT. Cells were then fixed with 4% formaldehyde in PBS for 10 minutes.

Microscopy

Live cells were imaged on an inverted microscope (Diaphot-300, Nikon) using a $40\times$ NA 1.3 oil Fluor or a $60\times$ NA 1.4 oil plan-Apo objective (Nikon). Fixed cells were imaged on an upright microscope (Axioplan 2; Carl Zeiss MicroImaging) using a $63\times$ NA 1.4 oil plan-Apochromat objective (Carl Zeiss MicroImaging, Inc). All images were collected with a cooled back-thinned CCD camera (MicroMax 512BFT; Princeton Instruments) with a $2\times$ optovar attached using MetaMorph software (Molecular Devices). For population data, 20–40 randomly selected cells were imaged per coverslip. In order to collect velocity data, live cells were imaged twice, 30 seconds apart. Individual cells were imaged at 2- or 5-second intervals for FSM or measurement of edge dynamics, respectively.

Cell Shape Analysis

Cell morphology was measured by representing cell shapes as polygons, as described [29,34]. Briefly, cell shapes were extracted manually from phase images using the Magnetic Lasso tool in Photoshop (Adobe) and saved as binary images. Using Celltool, an open source collection of tools for quantifying cell shape [34], polygonal cell outlines were extracted from the binary images and represented as two-dimensional splines, which were then resampled at 200 evenly spaced points to generate the final polygons. To measure cell edge velocities, 200-point polygons were extracted from long movies of individual cells. Displacement vectors between polygons extracted from successive image frames were calculated for each point. The edge velocity at each point was calculated by dividing the component of the displacement vector normal to the cell edge by the time interval at which the images were acquired (5 seconds). The polygon points were numbered for each frame such that the point at the front center of the leading edge was the first point of the polygon (point 0). To measure steady-state cell shapes for a large population of cells, polygons were extracted from a large population of cell images and mutually aligned. Principal modes of shape variation were determined by principal component analysis of the population of polygonal cell outlines, and scaled in terms of the standard deviation of the population for each mode of variation. In addition, cell area, aspect ratio, and left-right asymmetry were measured directly from the aligned polygons. Aspect ratio was measured by dividing the cell width (the cell axis perpendicular to the direction of movement) by the cell length (the cell axis parallel to the direction of movement). Left-right asymmetry was measured by dividing the length of the cell on one side of the cell body by the length of the cell on the other side with the greater length in the denominator, such that the asymmetry measurement was 1 or greater for all cells.

Measurement of Actin Network Flow

Movement of the actin network was measured using an adaptive multi-frame correlation algorithm as described [26]. Briefly, we

used 5-frame averaging (10 seconds) and a correlation template between 11×11 and 21×21 pixels. This method assumes steady-state movement of the actin network within the area of the correlation template over the duration of the temporal window, but keratocytes move too quickly to meet this requirement. Thus, image sequences were converted from the laboratory frame of reference to the cell frame of reference prior to flow tracking [66]. The flow measurements were performed in the cell frame of reference and the resulting flow maps were then transformed back to the laboratory frame of reference. Also, phalloidin speckles were accentuated by applying a spatial band-pass filter to the images before flow tracking.

Mathematical Modeling

The model consists of coupled sub-models for (i) viscous flow of the F-actin network, (ii) myosin transport, (iii) adhesion density and (iv) F-actin density. We solved the equations of these sub-models (described in detail in Text S1) for different values for the adhesion drag coefficient using the GPL-licensed software FreeFem++ (available for download at <http://www.freefem.org>) designed to solve partial difference equations using finite element methods. To dynamically compute cell shape, we used the following iteration procedure: at each iteration step, myosin, F-actin, and adhesion densities and centripetal actin flow were simulated until all densities and the flow reached steady state. Then, the boundary mesh was advanced/retracted using the forward Euler method in the locally normal direction with the rate $v(s) = V_p(s) + U_{\perp}(s)$, where $U_{\perp}(s)$ is the normal component of the simulated flow pattern \vec{U} at the cell boundary and $V_p(s)$ is the rate of actin polymerization. After the shape change, the lamellipodial area was remeshed and the density and flow simulations were repeated until the iterations converged to a stable shape.

Supporting Information

Figure S1 Cell-substrate adhesion strength increases with increasing PLL-PEG-RGD concentration. Keratocytes plated on glass coverslips coated with a range of PLL-PEG-RGD concentrations were centrifuged, upside down, at $1600 \times g$ for 10 minutes. The number of cells attached to each surface was counted before and after centrifugation, and the average percentage of cells that remained attached following centrifugation for three trials is plotted versus PLL-PEG-RGD concentration. Error bars indicate standard error of the mean. (TIF)

Figure S2 Variations in cell shape increase at high adhesion strengths. Front velocity, area, aspect ratio, and left-right asymmetry are plotted over time for individual cells plated on low (top row), intermediate (middle row), and high (bottom row) adhesion strength surfaces (0.8, 4, and $500 \mu\text{g/ml}$ PLL-PEG-RGD, respectively). $N = 8$ cells for each population; each individual cell within the three populations is represented by a distinct line color for all four measurements. The thick red lines indicate the cells shown in Figure 2. (TIF)

Figure S3 Simulated myosin and retrograde flow patterns for a generic input cell shape. Coupled myosin and flow distributions were computed on a fixed, generic cell shape at low (left), medium (center) and high (right) adhesion strengths. (A) Simulated myosin distributions. (B) Simulated actin retrograde flow maps. Color-coded arrows show local flow direction and magnitude (hot colors correspond to faster flow). (C) Distributions of the computed normal component of the centripetal flow around

the boundary (blue), polymerization rate (red) and net protrusion/retraction rate (black). (TIF)

Figure S4 Simulated adhesion and actin filament distribution patterns for a generic input cell shape. Coupled adhesions and actin distributions were computed on a fixed, generic cell shape at low (left), medium (center) and high (right) adhesion strengths. (A) Simulated adhesion distributions. (B) Simulated F-actin distributions. (C) Distributions of the computed adhesion (green) and F-actin (red) densities around the cell boundary. Units are non-dimensionalized (n.d). (TIF)

Figure S5 Simulated actin network flow patterns for different adhesion strengths and myosin activities. Nine cell shapes correspond to nine conditions: low, medium, and high adhesion (left, center and right column, respectively) and blebbistatin-treated, control and calyculin-treated cells (lower, center and top row, respectively). Actin retrograde flow was simulated for the nine different cell shapes using the indicated values for the adhesion drag coefficient ζ and the myosin force coefficient k . See Text S1 for a list of all parameter values. Local flow is indicated by color-coded arrows (hot colors correspond to faster flow). (TIF)

Figure S6 The effects of calyculin A on cell speed and area are reduced when myosin contraction is inhibited with blebbistatin. Histograms that display the distribution of cell speed and area are shown for control cells (A) as well as cells treated with $10 \mu\text{M}$ blebbistatin (B), 10 nM calyculin A (C), or $10 \mu\text{M}$ blebbistatin + 10 nM calyculin A (D). (TIF)

Figure S7 Average measured actin network flow rates at varying adhesion and myosin strengths. Average actin polymerization rates (red lines) and actin retrograde flow rates (blue lines) measured in populations of cells treated with calyculin A (top row) or blebbistatin (bottom row) are plotted for each point around the cell perimeter. The gray lines are the effective expansion/retraction rates calculated by adding the measured actin polymerization and retrograde flow rates. Error bars indicate standard error of the mean. Measurements from control cells, shown in Figure 6, are shown here for comparison (middle row). (TIF)

Figure S8 Simulated actin network flow maps and myosin, adhesion, and actin distributions for the case where the adhesion drag coefficient ζ decreases with increasing adhesion density. (A) Spatial distribution of the adhesion drag coefficient ζ . (B) Simulated myosin distributions. (C) Simulated actin retrograde flow maps. The direction and magnitude of actin network movement with respect to the underlying substrate is indicated color-coded arrows; hot colors correspond to faster flow. (D) Distributions of the computed normal component of the centripetal flow around the cell boundary (blue), polymerization rate (red), and net expansion/retraction rate (black). The centripetal flow rates at the cell boundary were taken from the simulated flow maps shown in part B. The actin polymerization rates are the rates required to maintain the input cell shape, given the simulated retrograde flow patterns. (E) Simulated adhesion distributions. (F) Simulated actin distributions. (G) Distributions of the computed adhesion (green) and actin (red) densities around the cell perimeter. Units are non-dimensionalized (n.d.). See Text S1 for simulation parameters. (TIF)

Figure S9 Simulated actin network flow maps and myosin, adhesion, and actin distributions for the case where the adhesion drag coefficient ζ increases with increasing adhesion density. (A) Spatial distribution of the adhesion drag coefficient ζ . (B) Simulated myosin distributions. (C) Simulated actin retrograde flow maps. The direction and magnitude of actin network movement with respect to the underlying substrate is indicated color-coded arrows; hot colors correspond to faster flow. (D) Distributions of the computed normal component of the centripetal flow around the cell boundary (blue), polymerization rate (red), and net expansion/retraction rate (black). The centripetal flow rates at the cell boundary were taken from the simulated flow maps shown in part (B). The actin polymerization rates are the rates required to maintain the input cell shape, given the simulated retrograde flow patterns. (E) Simulated adhesion distributions. (F) Simulated actin distributions. (G) Distributions of the computed adhesion (green) and actin (red) densities around the cell perimeter. Units are non-dimensionalized (n.d.). See Text S1 for simulation parameters.
(TIF)

Movie S1 A keratocyte crawling at intermediate adhesion strength. The cell is crawling on a glass surface coated with 4 $\mu\text{g/ml}$ PLL-PEG-RGD. The cell is fan-shaped, with clearly defined lead and trailing edges, and moves persistently in one direction. The movie is at 30 \times real time.
(MOV)

Movie S2 A keratocyte crawling at low adhesion strength. The cell is crawling on a glass surface coated with 0.8 $\mu\text{g/ml}$ PLL-PEG-RGD. The cell is round and exhibits noisier protrusion and retraction, compared to the cell in Movie S1. The movie is at 30 \times real time.
(MOV)

Movie S3 A keratocyte crawling at high adhesion strength. The cell is crawling on a glass surface coated with 500 $\mu\text{g/ml}$ PLL-PEG-RGD. The cell exhibits traveling waves of protrusion along the leading edge. The movie is at 30 \times real time.
(MOV)

Movie S4 An individual cell transitions between low and intermediate adhesion strength migration behaviors. The cell is crawling on a micro-patterned surface, where the light region has been stamped with an intermediate concentration of PLL-PEG-RGD and the dark region has been back-filled with a lower concentration. Cell area and aspect ratio increase as the cell crosses from the low adhesion region to the intermediate adhesion region. The movie is at 30 \times real time.
(MOV)

Movie S5 An individual cell transitions between intermediate and high adhesion strength migration behaviors. The cell is crawling on a micro-patterned surface, where the light region has been stamped with a high concentration of PLL-PEG-RGD and the dark region has been back-filled with an intermediate concentration. The cell exhibits protrusion waves immediately after crawling onto the high adhesion region. The movie is at 30 \times real time.
(MOV)

References

1. Keren K, Theriot JA (2008) Biophysical aspects of actin-based cell motility in fish epithelial keratocytes. *Cell Motility*. pp 31–58.

Movie S6 Dynamical simulations of cell shape for different adhesion drag coefficients recapitulate experimentally observed differences in cell shape. Cell shape and actin network flow were simulated using an iteration procedure: myosin densities and centripetal actin flow were simulated until the myosin distribution and the flow pattern reached steady state (see Text S1). Then, the boundary mesh was advanced/retracted in the locally normal direction with the rate $v(s) = V_p(s) + U_{\perp}(s)$, where $U_{\perp}(s)$ is the normal component of the simulated flow pattern \vec{U} at the cell boundary and $V_p(s)$ is the rate of actin polymerization. After the shape change, the lamellipodial area was remeshed and the density and flow simulations were repeated until the iterations converged to a stable shape. In the first half of the movie, the adhesion drag coefficient $\zeta = 0.04 \text{ nNs}/\mu\text{m}^4$ and the cell converges to a round shape. Halfway through the movie, ζ increases to $0.2 \text{ nNs}/\mu\text{m}^4$ and the shape evolves to a more elongated shape. The direction and magnitude of local actin network movement with respect to the underlying substrate is indicated by color-coded arrows; hot colors correspond to faster flow.
(MOV)

Table S1 Model variables.
(PDF)

Table S2 Constant model parameters.
(PDF)

Table S3 Model parameters dependent on adhesion strength.
(PDF)

Table S4 Model parameters dependent on myosin strength.
(PDF)

Table S5 Model parameters dependent on adhesion and myosin strength.
(PDF)

Text S1 Computational model of actin-myosin-adhesion mechanics.
(PDF)

Text S2 Supplemental results.
(PDF)

Acknowledgments

We are grateful to Zach Pincus for supplying Celltool, the software used to analyze cell shape, Cyrus Wilson and Gaudenz Danuser for providing the MatLab code used to track actin network movement in motile keratocytes, and Mark Tsuchida for help with the extraction protocol used for myosin II immunolabeling. We would also like to thank Natalie Dye and Kristina Godek for critical reading of the manuscript.

Author Contributions

The author(s) have made the following declarations about their contributions: Conceived and designed the experiments: ELB KK JAT. Performed the experiments: ELB. Analyzed the data: ELB KL AM. Wrote the paper: ELB KL AM JAT. Developed the model: AM KL ELB KK JAT. Performed model simulations: KL AM.

- collagen occurs at an intermediate attachment strength. *J Cell Biol* 122: 729–737.
3. Gupton SL, Waterman-Storer CM (2006) Spatiotemporal feedback between actomyosin and focal-adhesion systems optimizes rapid cell migration. *Cell* 125: 1361–1374.
 4. Huttenlocher A, Ginsberg MH, Horwitz AF (1996) Modulation of cell migration by integrin-mediated cytoskeletal linkages and ligand-binding affinity. *J Cell Biol* 134: 1551–1562.
 5. Palecek SP, Loftus JC, Ginsberg MH, Lauffenburger DA, Horwitz AF (1997) Integrin-ligand binding properties govern cell migration speed through cell-substratum adhesiveness. *Nature* 385: 537–540.
 6. Mitchison T, Kirschner M (1988) Cytoskeletal dynamics and nerve growth. *Neuron* 1: 761–772.
 7. Chan CE, Odde DJ (2008) Traction dynamics of filopodia on compliant substrates. *Science* 322: 1687–1691.
 8. DiMilla PA, Barbee K, Lauffenburger DA (1991) Mathematical model for the effects of adhesion and mechanics on cell migration speed. *Biophys J* 60: 15–37.
 9. Fournier MF, Sauser R, Ambrosi D, Meister JJ, Verkhovsky AB (2010) Force transmission in migrating cells. *J Cell Biol* 188: 287–297.
 10. Gardel ML, Sabass B, Ji L, Danuser G, Schwarz US, et al. (2008) Traction stress in focal adhesions correlates biphasically with actin retrograde flow speed. *J Cell Biol* 183: 999–1005.
 11. Hu K, Ji L, Applegate KT, Danuser G, Waterman-Storer CM (2007) Differential transmission of actin motion within focal adhesions. *Science* 315: 111–115.
 12. Bell GI (1978) Models for the specific adhesion of cells to cells. *Science* 200: 618–627.
 13. Zaidel-Bar R, Cohen M, Addadi L, Geiger B (2004) Hierarchical assembly of cell-matrix adhesion complexes. *Biochem Soc Trans* 32: 416–420.
 14. Nayal A, Webb DJ, Brown CM, Schaefer EM, Vicente-Manzanares M, et al. (2006) Paxillin phosphorylation at Ser273 localizes a GIT1-PIX-PAK complex and regulates adhesion and protrusion dynamics. *J Cell Biol* 173: 587–9.
 15. Miki H, Suetsugu S, Takenawa T (1998) WAVE, a novel wasp-family protein involved in actin reorganization induced by Rac. *EMBO J* 17: 6932–41.
 16. Miki H, Yamaguchi H, Suetsugu S, Takenawa T (2000) IRSP53 is an essential intermediate between Rac and WAVE in the regulation of membrane ruffling. *Nature* 408: 732–5.
 17. Stradal TEB, Scita G (2006) Protein complexes regulating Arp2/3-mediated actin assembly. *Curr Opin Cell Biol* 18: 4–10.
 18. Zhai J, Lin H, Nie Z, Wu J, Cañete-Soler R, et al. (2003) Direct interaction of focal adhesion kinase with p190RhoGEF. *J Biol Chem* 278: 24865–24873.
 19. Lim Y, Lim ST, Tomar A, Gardel M, Bernard-Trifilo JA, et al. (2008) PYK2 and FAK connections to p190Rho guanine nucleotide exchange factor regulate RhoA activity, focal adhesion formation, and cell motility. *J Cell Biol* 180: 187–203.
 20. Watanabe N, Kato T, Fujita A, Ishizaki T, Narumiya S (1999) Cooperation between mDial and ROCK in Rho-induced actin reorganization. *Nat Cell Biol* 1: 136–143.
 21. Kimura K, Ito M, Amano M, Chihara K, Fukata Y, et al. (1996) Regulation of myosin phosphatase by Rho and Rho-associated kinase (rho-kinase). *Science* 273: 245–8.
 22. Balaban NQ, Schwarz US, Riveline D, Gochberg P, Tzur G, et al. (2001) Force and focal adhesion assembly: a close relationship studied using elastic micropatterned substrates. *Nat Cell Biol* 3: 466–472.
 23. Riveline D, Zamir E, Balaban NQ, Schwarz US, Ishizaki T, et al. (2001) Focal contacts as mechanosensors: externally applied local mechanical force induces growth of focal contacts by an mDial-dependent and ROCK-independent mechanism. *J Cell Biol* 153: 1175–1186.
 24. Bershadsky AD, Balaban NQ, Geiger B (2003) Adhesion-dependent cell mechanosensitivity. *Annu Rev Cell Dev Biol* 19: 677–695.
 25. Svitkina TM, Verkhovsky AB, McQuade KM, Borisy GG (1997) Analysis of the actin-myosin II system in fish epidermal keratocytes: mechanism of cell body translocation. *J Cell Biol* 139: 397–415.
 26. Wilson CA, Tsuchida MA, Allen GM, Barnhart EL, Applegate KT, et al. (2010) Myosin II contributes to cell-scale actin network treadmill through network disassembly. *Nature* 465: 373–377.
 27. Lee J, Ishihara A, Theriot JA, Jacobson K (1993) Principles of locomotion for simple-shaped cells. *Nature* 362: 167–171.
 28. Mogilner A, Keren K (2009) The shape of motile cells. *Curr Biol* 19: R762–71.
 29. Keren K, Pincus Z, Allen GM, Barnhart EL, Marriott G, et al. (2008) Mechanism of shape determination in motile cells. *Nature* 453: 475–480.
 30. Lacayo CI, Pincus Z, VanDuijn MM, Wilson CA, Fletcher DA, et al. (2007) Emergence of large-scale cell morphology and movement from local actin filament growth dynamics. *PLoS Biol* 5: e233. doi:10.1371/journal.pbio.0050233.
 31. Lee J, Ishihara A, Oxford G, Johnson B, Jacobson K (1999) Regulation of cell movement is mediated by stretch-activated calcium channels. *Nature* 400: 382–386.
 32. Ream RA, Theriot JA, Somero GN (2003) Influences of thermal acclimation and acute temperature change on the motility of epithelial wound-healing cells (keratocytes) of tropical, temperate and Antarctic fish. *J Exp Biol* 206: 4539–4551.
 33. Goodrich HB (1924) Cell behavior in tissue cultures. *Biological Bulletin* 46: 252–262.
 34. Pincus Z, Theriot JA (2007) Comparison of quantitative methods for cell-shape analysis. *J Microsc* 227: 140–156.
 35. VandeVondele S, Voros J, Hubbell JA (2003) RGD-grafted poly-L-lysine-graft-(polyethylene glycol) copolymers block non-specific protein adsorption while promoting cell adhesion. *Biotechnol Bioeng* 82: 784–790.
 36. Pierschbacher MD, Ruoslahti E (1984) Cell attachment activity of fibronectin can be duplicated by small synthetic fragments of the molecule. *Nature* 309: 30–33.
 37. Ruoslahti E (1996) RGD and other recognition sequences for integrins. *Annu Rev Cell Dev Biol* 12: 697–715.
 38. Rubinstein B, Fournier MF, Jacobson K, Verkhovsky AB, Mogilner A (2009) Actin-myosin viscoelastic flow in the keratocyte lamellipod. *Biophys J* 97: 1853–1863.
 39. Straight AF, Cheung A, Limouze J, Chen I, Westwood NJ, et al. (2003) Dissecting temporal and spatial control of cytokinesis with a myosin II inhibitor. *Science* 299: 1743–1747.
 40. Ishihara H, Ozaki H, Sato K, Hori M, Karaki H, et al. (1989) Calcium-independent activation of contractile apparatus in smooth muscle by calyculin-A. *J Pharmacol Exp Ther* 250: 388–396.
 41. Anderson KI, Cross R (2000) Contact dynamics during keratocyte motility. *Curr Biol* 10: 253–260.
 42. Lee J, Jacobson K (1997) The composition and dynamics of cell-substratum adhesions in locomoting fish keratocytes. *J Cell Sci* 110(Pt 22): 2833–2844.
 43. Cirit M, Krajcovic M, Choi CK, Wolf ES, Horwitz AF, et al. (2010) Stochastic model of integrin-mediated signaling and adhesion dynamics at the leading edges of migrating cells. *PLoS Comput Biol* 6: doi:10.1371/journal.pcbi.1000688.
 44. Beninger KA, Dembo M, Kaverina I, Small JV, Wang YL (2001) Nascent focal adhesions are responsible for the generation of strong propulsive forces in migrating fibroblasts. *J Cell Biol* 153: 881–888.
 45. Zaidel-Bar R, Itzkovitz S, Ma'ayan A, Iyengar R, Geiger B (2007) Functional atlas of the integrin adhesome. *Nat Cell Biol* 9: 858–867.
 46. Macdonald A, Horwitz AR, Lauffenburger DA (2008) Kinetic model for lamellipodial actin-integrin ‘clutch’ dynamics. *Cell Adh Migr* 2: 95–105.
 47. Butler B, Gao C, Mersich AT, Blystone SD (2006) Purified integrin adhesion complexes exhibit actin-polymerization activity. *Curr Biol* 16: 242–251.
 48. Endlich N, Otey CA, Kriz W, Endlich K (2007) Movement of stress fibers away from focal adhesions identifies focal adhesions as sites of stress fiber assembly in stationary cells. *Cell Motil Cytoskeleton* 64: 966–976.
 49. Hotulainen P, Lappalainen P (2006) Stress fibers are generated by two distinct actin assembly mechanisms in motile cells. *J Cell Biol* 173: 383–394.
 50. Mogilner A, Oster G (1996) Cell motility driven by actin polymerization. *Biophys J* 71: 3030–3045.
 51. Pollard TD, Borisy GG (2003) Cellular motility driven by assembly and disassembly of actin filaments. *Cell* 112: 453–465.
 52. Renkawitz J, Schumann K, Weber M, Lammemann T, Picke H, et al. (2009) Adaptive force transmission in amoeboid cell migration. *Nat Cell Biol* 11: 1438–1443.
 53. Yam PT, Wilson CA, Ji L, Hebert B, Barnhart EL, et al. (2007) Actin-myosin network reorganization breaks symmetry at the cell rear to spontaneously initiate polarized cell motility. *J Cell Biol* 178: 1207–1221.
 54. Barnhart EL, Allen GM, Julicher F, Theriot JA (2010) Bipedal locomotion in crawling cells. *Biophys J* 98: 933–942.
 55. Del Alamo JC, Meili R, Alonso-Latorre B, Rodriguez-Rodriguez J, Aliseda A, et al. (2007) Spatiotemporal analysis of eukaryotic cell motility by improved force cytometry. *Proc Natl Acad Sci U S A* 104: 13343–13348.
 56. Dobreiner HG, Dubin-Thaler BJ, Hofman JM, Xenias HS, Sims TN, et al. (2006) Lateral membrane waves constitute a universal dynamic pattern of motile cells. *Phys Rev Lett* 97: 038102.
 57. Giannone G, Dubin-Thaler BJ, Dobreiner HG, Kieffer N, Bresnick AR, et al. (2004) Periodic lamellipodial contractions correlate with rearward actin waves. *Cell* 116: 431–443.
 58. Giannone G, Dubin-Thaler BJ, Rossier O, Cai Y, Chaga O, et al. (2007) Lamellipodial actin mechanically links myosin activity with adhesion-site formation. *Cell* 128: 561–575.
 59. Machacek M, Danuser G (2006) Morphodynamic profiling of protrusion phenotypes. *Biophys J* 90: 1439–1452.
 60. Machacek M, Hodgson L, Welch C, Elliott H, Pertz O, et al. (2009) Coordination of Rho GTPase activities during cell protrusion. *Nature* 461: 99–103.
 61. Weiner OD, Marganski WA, Wu LF, Altschuler SJ, Kirschner MW (2007) An actin-based wave generator organizes cell motility. *PLoS Biol* 5: e221. doi:10.1371/journal.pbio.0050221.
 62. Bosgraaf L, Haastert PJMV (2009) The ordered extension of pseudopodia by amoeboid cells in the absence of external cues. *PLoS ONE* 4: e5253. doi:10.1371/journal.pone.0005253.
 63. Satulovsky J, Lui R, Wang YL (2008) Exploring the control circuit of cell migration by mathematical modeling. *Biophys J* 94: 3671–3683.
 64. Csucs G, Michel R, Lussi JW, Textor M, Danuser G (2003) Microcontact printing of novel copolymers in combination with proteins for cell-biological applications. *Biomaterials* 24: 1713–1720.
 65. Whitesides GM, Ostuni E, Takayama S, Jiang X, Ingber DE (2001) Soft lithography in biology and biochemistry. *Annu Rev Biomed Eng* 3: 335–373.
 66. Wilson CA, Theriot JA (2006) A correlation-based approach to calculate rotation and translation of moving cells. *IEEE Trans Image Process* 15: 1939–1951.

Text S1

Computational model of actin-myosin-adhesion mechanics

Myosin-powered retrograde actin network flow

Experimental and theoretical studies have established that myosin contracts actin arrays and generates contractile stress and that this stress grows with increasing myosin concentration [1, 2]. For simplicity in our model, we neglect the possibility that the myosin stress could be anisotropic, consider it a scalar and make the simplest assumption that the stress, kM , is linearly proportional to the myosin density. Here M is the myosin density and k is the proportionality coefficient (typical force per myosin unit) that depends on blebbistatin/calyculin treatment. The contractile force applied to the actin network is the divergence of the stress, in this case, its gradient, $k\nabla M$. Following [3] we assume that adhesion complexes generate viscous resistance to the flow of F-actin (with velocity \vec{U} in the lab coordinate system). The respective resistance force, $\zeta\vec{U}$, where ζ is the effective drag coefficient that we call adhesion strength, is balanced by the active contractile stress: $\zeta\vec{U} = k\nabla M$.

The simple equation $\zeta\vec{U} = k\nabla M$ does not take into account passive stresses in the F-actin network due to its deformation during the flow. To add these passive stresses, we follow [3] and assume that these stresses have viscous character on the relevant time scale of tens of seconds. The small elastic component of the stress in the lamellipodium can be neglected [3], so we model a combination of the shear and deformation stresses in the F-actin with the formula $(\mu_b - \frac{2}{3}\mu)(\nabla \cdot \vec{U})I + \mu(\nabla\vec{U} + (\nabla\vec{U})^T)$, where μ and μ_b are the shear and bulk viscosities, respectively, and I is the identity tensor. Adding the divergence of these passive stresses to the myosin and adhesion forces results in the force balance equation determining the flow rate:

$$\left[\left(\frac{1}{3}\mu + \mu_b \right) \nabla \nabla \cdot \vec{U} + \mu \nabla^2 \vec{U} \right] + k \nabla M = \zeta \vec{U} \quad (1)$$

The boundary condition is the zero pressure at the free lamellipodial boundary:

$$\vec{n} \left[\left(\mu_b - \frac{2}{3}\mu \right) (\nabla \cdot \vec{U}) I + \mu (\nabla \vec{U} + (\nabla \vec{U})^T) + kM \right] = 0 \quad (2)$$

Here \vec{n} is local normal unit vector to the lamellipodial boundary. This model assumes that the F-actin

viscosity is spatially constant, independent of the F-actin density, which simplifies the analysis. A more detailed assumption of the viscosity being a function of the F-actin density does not change the qualitative pattern of the actin flow [3].

We also assume that there is a small pressure δ at the cell body boundary (shown as the circular domain inside the lamellipodium):

$$\vec{n} \left[\left(\mu_b - \frac{2}{3}\mu \right) (\nabla \cdot \vec{U}) I + \mu (\nabla \vec{U} + (\nabla \vec{U})^T) + kM \right] = \delta \quad (3)$$

The rationale for such pressure is that the cell body is squeezed at the top by the membrane tension, so the cell body tends to expand to the sides and compress the underlying actin gel. This pressure is not critical: without it (if $\delta = 0$) all results are valid, except the predicted actin flow at the center of the rear becomes a bit too fast. There are no constraints on the flow velocity at the cell body boundary.

Adhesion strength

Cell-substrate adhesion is thought to be mediated by a mechanism in which adhesion molecules act as “molecular clutches” that couple the actin network to the underlying substrate [4, 5]. The strength of cell-substrate adhesion, which in our model is described by the adhesion drag coefficient ζ , depends on the number of clutches bound to both the actin network and the substrate. Cell-substrate adhesion is mediated by integrin binding of extracellular matrix proteins, and so ζ depends on the density of integrin molecules and the integrin binding affinity for both the ECM on the outside of the cell and for additional adhesion proteins that link integrins to the actin network on the inside of the cell. The spatial distribution of integrin density and affinity states has not been well-characterized in keratocytes, and so as a first pass, we make the simple assumption that ζ is spatially constant (Figures 5, 9, and 11 in the main text). However, the spatial distribution of mature adhesions, as marked by the adhesion protein vinculin, is heterogeneous (see Figure 10 in the main text). The relationship between the size and age of adhesions and adhesion strength has not been well characterized. The simplest possibility is that increased density of adhesion molecules correlates with a higher density of molecular bonds and protein friction. Alternatively, increased density of integrin $\alpha_V\beta_3$ in older adhesions has been shown to be correlated with increased turnover of integrin $\alpha_V\beta_3$ in the cell rear in migrating mouse melanoma cells [6] and estimates of adhesion strength in migrating keratocytes suggest that adhesion strength is greater in the front of the cell [7], despite increased densities of adhesion proteins in the cell rear [8, 9]. Therefore, we have considered both the case where the magnitude of ζ decreases with increasing adhesion density and the case where ζ increases

with increasing adhesion density (Supplemental Figures 8 and 9, respectively). In the case where adhesion strength decreases with adhesion density, the adhesion friction coefficient $\zeta = \zeta_{small} + \frac{2\zeta_0}{1+(A/A_\zeta)^2}$, where ζ_{small} is the minimal friction coefficient, ζ_0 equals to the value of ζ for the homogeneous model, A_ζ sets the threshold adhesion density at which ζ is strongly affected by the adhesion density, and A is the adhesion density (see the model for adhesion dynamics below). For the case where adhesion strength increases with adhesion density, $\zeta = \zeta_{small} + \frac{2\zeta_0(A/A_\zeta)^2}{1+(A/A_\zeta)^2}$.

Myosin transport

Following [3], we assume that myosin molecules associate and move with the F-actin network. Myosin molecules detach from the F-actin, diffuse in the cytoplasm and reattach. Here, we assume that detachment and reattachment is rapid, in which case the system of equations for the actin-associated and diffusing myosin molecules [3] reduces to just one equation for the actin-associated myosin, in which the rapid cycles of the detachment, diffusion in the cytoplasm and reattachment effectively result in slow diffusion of the actin-associated myosin added to the myosin movement due to coupling with the F-actin:

$$\frac{\partial M}{\partial t} = D_M \nabla^2 M - \nabla \cdot ((\vec{U} - \vec{V}_{cell})M) \quad (4)$$

Here D_M is the effective diffusion coefficient, and \vec{V}_{cell} is the velocity of the cell migration. Note that we calculate the myosin distribution in the framework of the moving cell. In the cell frame of reference, the F-actin moves backward with speed V_{cell} as well as flowing centripetally with velocity \vec{U} . Myosin moves with the local actin network velocity, so the vector sum of V_{cell} and \vec{U} gives the net drift rate for myosin. The boundary condition for the myosin transport is the zero flux of myosin through the lamellipodial boundary:

$$\vec{n} \cdot [D_M \nabla M - M(\vec{U} - \vec{V}_{cell})] = 0 \quad (5)$$

This formulation is valid if the the majority of myosin molecules are attached to the actin network and move with the actin network, as previously demonstrated for keratocytes (Svitkina et al., 1997). The effective diffusion rate and explicit processes of myosin turnover are not crucial for the model results.

Adhesion dynamics

We assume that adhesion molecular complexes (described by the density A) appear across the lamellipodium with the constant rate S_A and disassemble with the constant rate γ . Furthermore, following [10], we assume that there is slippage between molecules of the adhesion complexes, so the adhesion complexes are dragged on the surface by the F-actin flow with the velocity $\vartheta\vec{U}$ which is collinear with the F-actin flow but is slower ($0 < \vartheta < 1$ is the flow-coupling coefficient). For numerical stability, to smoothen the adhesion distribution, we add a slow diffusion of the adhesion complexes with the small diffusion coefficient D_A . Besides the computational advantage, the diffusion term reflects small stochastic displacements of the adhesion molecules. Thus, the adhesion density in the cell frame is governed by the equation:

$$\frac{\partial A}{\partial t} = D_A \nabla^2 A - \nabla \cdot ((\vartheta\vec{U} - \vec{V}_{cell})A) + S_A - \gamma A \quad (6)$$

A kinematic argument similar to that for the myosin sub-model explains the drift rate $(\vartheta\vec{U} - \vec{V}_{cell})$ of the adhesions, and also similarly to the myosin case, the boundary condition is the zero flux:

$$\vec{n} \cdot [D_A \nabla A - A(\vartheta\vec{U} - \vec{V}_{cell})] = 0 \quad (7)$$

Note that this sub-model computes the adhesion *density* distribution rather than the distribution of mechanical adhesion *strength*. The relationship between adhesion density distribution and mechanical adhesion strength is described above.

F-actin dynamics

The F-actin (density a) drifts with velocity $(\vec{U} - \vec{V}_{cell})$ in the moving cell framework and disassembles across the lamellipodium with the rate v . Myosin contraction has been shown to accelerate the disassembly of the F-actin network [11], so we assume that v increases with increasing myosin contraction. For numerical stability, to smoothen the actin distribution, we add a slow diffusion characterized by the small diffusion coefficient D_a to the actin drift. Besides the computational advantage, the diffusion term reflects small stochastic fluctuations of the actin filaments. The F-actin density in the cell frame is described by the equation:

$$\frac{\partial a}{\partial t} = D_a \nabla^2 a - \nabla \cdot \left((\vec{U} - \vec{V}_{cell}) a \right) - va (1 + (M/M_0)) \quad (8)$$

We assume that actin filaments assemble at the lamellipodial edge with a rate affected by antagonism between adhesions and the branched actin network [12, 13]. Specifically, we use the formula:

$$\vec{n} \cdot \left[D_a \nabla a - a (\vec{U} - \vec{V}_{cell}) \right] = \frac{\alpha}{1 + (A/A_0)} \quad (9)$$

Here, the right side of the equation describes the influx of F-actin at the boundary, α , which is inhibited by the adhesion density (factor in the denominator).

Model parameters

The model variables and parameters are listed in Tables I-V. For the actin flow sub-model, we use the parameter values estimated for the keratocyte lamellipodium in (Rubinstein et al. 2009). We use a typical value for the shear viscosity, $\mu = 2 \text{ kPa} \times \text{s}$. The bulk viscosity is normally higher than the shear viscosity, as the gels are more resistant to compression than shear. We use the value $\mu_b = 100 \text{ kPa} \times \text{s}$. In order for the myosin stress to generate the observed flow of the order of $\sim 0.1 \text{ } \mu\text{m/s}$, the stress has to be $\sim 100 \text{ pN}/\mu\text{m}^2$, which is also realistic considering known estimates of the traction force and number of myosin molecules. Thus, we use the force $k = 100 \text{ pN}$. In the calculations, we multiply the viscosities and parameter k by the characteristic thickness of the lamellipodium $h = 0.2 \text{ } \mu\text{m}$ in order to convert the 3D stress derivatives into the 2D surface force densities. For the adhesion drag coefficient, we use $\zeta = 0.2 \text{ nN} \times \text{s}/\mu\text{m}^4$, of the same order of magnitude as the estimate in [3]. To non-dimensionalize the equations, we choose the characteristic lamellipodial size, $\sim 10 \text{ } \mu\text{m}$, as the scale of distance and the cell speed, $\sim 0.2 \text{ } \mu\text{m/s}$ as the scale of the velocity, so $10 \text{ } \mu\text{m}/0.2 \text{ } \mu\text{m/s} \sim 50 \text{ s}$ is the scale of time. We choose $\mu h \vec{V}_{cell} \sim 100 \text{ pN}$ as the scale of force.

We use the total amount of myosin $\bar{M} = 55$ of non-dimensional units, so that the average myosin density (total myosin divided by the cell area) multiplied by the characteristic myosin force per square micron gives typical known contractile stress. Note that the total amount of myosin is conserved in the model: when the cell area goes up/down compared to the control, the average myosin density decreases/increases. We used the diffusion terms $D_M = 0.8 \text{ } \mu\text{m}^2/\text{s}$, $D_A = 0.2 \text{ } \mu\text{m}^2/\text{s}$ and $D_a = 0.2 \text{ } \mu\text{m}^2/\text{s}$ which guaranteed that the diffusion terms were significantly smaller than the drift terms.

The observations indicate that many individual adhesion complexes disappear within the lamellipodium, but many others survive from the front to the rear, so we chose the adhesion disassembly rate $\gamma = 1/150$ s, comparable but higher than the inverse characteristic time for the cell migration. In order to maintain the non-dimensionalized adhesion density of the order of 1, we use the adhesion assembly rate $S_A = 1$ unit/50 s. We chose the flow-coupling coefficient $\varphi = 0.4$ assuming that the adhesion molecules on the average slip to comparable degrees relative to the surface and actin network.

Multiple observations suggest that the F-actin disassembles within tens of seconds in the lamellipodium [11], so we choose the actin disassembly rate $v = 1/50$ s. In order to maintain the non-dimensionalized actin density of the order of 1, we use the actin assembly rate $\alpha = 0.4$ units $\times\mu\text{m}/\text{s}$. Numerical experiments showed that a realistic spatial F-actin distribution evolves if the threshold myosin amount that significantly accelerates actin disassembly is $M_0 = 20$, and the characteristic adhesion density affecting actin assembly is $A_0 = 1$.

The parameters above are for the control cells. For low/high adhesion, the parameter ζ was decreased/increased as shown in Table III. Similarly, when myosin was inhibited/enhanced, the parameter k was lowered/elevated as shown in Table IV. We changed the flow-coupling coefficient to 0.9 and 0.2 for low/high adhesion conditions, respectively, assuming that as adhesion strength increases, adhesion molecules associated more tightly with the surface and slip more relative to the actin network. The adhesion disassembly rate was increased to 1/50 s and decreased to 1/250 s for low/high adhesion conditions, respectively. The actin disassembly rate was decreased to 1/100 s for high adhesion conditions; otherwise, the actin density decreases too much in the cell interior due to the very slow centripetal flow. Perhaps higher adhesion contributes to enhanced stability of existing actin filaments. Finally, multiple numerical experiments demonstrated that realistic actin distributions are achieved if myosin affects actin depolymerization less at both low and high adhesion compared to the control case (Table III).

In the simulations, we used various cell areas and speeds given by the experimental measurements for the nine conditions (Table V).

Simulation of actin-myosin-adhesion dynamics and predicting respective densities

We generated numerically fixed cell shapes similar to those observed experimentally, and used the LGPL-licensed software FreeFem++ (designed to solve Partial Differential Equations using finite element methods; available for download at www.freefem.org) to solve Eqs. 1-8 as follows. First, Eqs. 1-5 for flow velocities

and myosin distributions were solved numerically with initial conditions of uniformly spread myosin and zero flow, resulting, after transients decreased almost to zero, in a stable myosin distribution $M(\vec{r})$ and flow field $\vec{U}(\vec{r})$. Then, using the resulting steady flow field, we solved Eqs. 6-7 to find the stable adhesion distribution $A(\vec{r})$. Finally, using the resulting steady flow field and myosin and adhesion distributions, we solved Eqs. 8-9 to find the stable F-actin distribution $a(\vec{r})$.

Prediction of the polymerization rate and net protrusion/retraction rate

We assume that the cell boundary is determined by the Graded Radial Extension model [14]: the rate of the net protrusion and retraction of the boundary is graded, and in the steady state, the cell shape is determined by the angle between the local normal vector to the cell boundary and the direction of the cell migration $\theta(s)$, which is related to the protrusion/retraction rate, $v(s)$, by the formula:

$$\cos(\theta(s)) = v(s)/v(0) \quad (10)$$

Here s is the arc length along the cell boundary; we calibrate it so that $s = 0$ corresponds to the center front, $s = \pm 50$ corresponds to the sides, and $s = \pm 100$ corresponds to the center rear. An additional constrain is that $v(0) = V_{cell}$. Thus, we calculate the graded protrusion/retraction rate for a given cell shape using the formula:

$$v(s) = V_{cell} \cos(\theta(s)) \quad (11)$$

Then, from the computed centripetal flow \vec{U} at the boundary, we find the projection of the flow onto the inward normal to the cell boundary, $U_{\perp} = -\vec{U} \cdot \vec{n}$, and note that the protrusion/retraction rate, $v(s) = V_p(s) + U_{\perp}(s)$, where v_p is the actin polymerization rate. Thus,

$$V_p(s) = v(s) - U_{\perp}(s) \quad (12)$$

We use Eqs. 10-11 to calculate the net protrusion/retraction rate and actin polymerization rates for given cell shapes.

Dynamic cell shape

According to [13], the actin polymerization rate, according to model, is given by the formula: $V_p(s) = V_0 \times (1 - \frac{T}{f_{stall}D(s)})^w$, where V_0 is the free polymerization rate proportional to the G-actin density, f_{stall} is the stall force per filament, T is the membrane tension, $w \gg 1$ is the parameter characterizing the force-velocity relation for actin filaments, and $D(s)$ is the local density of the pushing barbed ends proportional to the F-actin density at the boundary. Because of the strong inequality $w \gg 1$ (previously published experiments suggest that $w \sim 8$ [13]), the polymerization rate is predicted to be a step-function-like along the leading edge: almost constant along the front and dropping abruptly to very small values at the sides and rear. This prediction is in agreement with both our calculations (Figure 5) and experimental data (Figure 7). The membrane tension T , which at the moment we cannot measure directly, is the parameter regulating where along the boundary the polymerization rate drops.

In addition, the membrane tension, lamellipodial area and adhesion strength are interdependent: according to the observations, the area increases with the adhesion strength. We assume that the reason is the more significant adhesion free energy decrease when the lamellipodium spreads on stronger adhesion surfaces [15]. At the same time, greater lamellipodium spreading likely comes at the expense of pulling the plasma membrane off the cell body (causing squeezing of the cell body) and dynamic shift of the equilibrium between the intracellular and plasma membrane toward the greater plasma membrane area, which causes an increase of the membrane tension [16].

Thus, to simulate the cell shape dynamically, we assume: (i) There is a constant target cell area at given adhesion strength (the area is an increasing function of the adhesion strength). (ii) When area increases, the membrane tension increases, and the protrusion decreases. Specifically, we approximate the polymerization rate along the boundary with the function:

$$V_p(s) = V_0 \times g(s) + p(A) \tag{13}$$

Here $g(s)$ is a smoothed step-function: it is equal to 1 at the leading edge up to the middle of the sides, and equal to zero at the rear. The term $p(A)$ is constant along the boundary and represents a small additional polymerization at the rear and front. However, this constant depends on the cell area: it decreases when the cell area increases. Also, this constant increases with the adhesion strength which leads to the increase of the equilibrium cell area with the adhesion strength. The function $p(A)$ is calibrated so that the target area of the cell stays constant in the dynamic simulations. In the future, we will upgrade the model by introducing a more detailed dependence of the polymerization rate on the membrane tension

and area.

Using these assumptions, the dynamic iterative procedure of the cell shape simulation is as follows: 1) We solved coupled Eqs. 1-4 on a given cell shape until the steady stable myosin and flow distributions evolved. 2) From the steady centripetal flow distribution \vec{U} at the boundary, we computed the projection of the flow onto the inward normal to the cell boundary, U_{\perp} , and the protrusion/retraction rate, $v(s) = V_p(s) + U_{\perp}(s)$, where V_p is given by Eq. 12. Parameter $p(A)$ was adjusted to keep the cell area constant. 3) We evolved the cell boundary using the computed rate $v(s)$ (by using forward Euler method to displace nodes of the discrete grid on the boundary). 4) We re-meshed the boundary and the 2D domain encircled by it and repeated the steps 1-3. Repeating this iterative procedure led to convergence of the cell shape to a stable one.

Model Results

From dimensional and linear stability analysis of the coupled actin-myosin-adhesion dynamics, we conclude that the order of magnitude of the centripetal flow of actin turns out to be $\sim \frac{kM}{\sqrt{\zeta\mu_b}}$. Thus, the flow is proportional to the myosin strength, and is a decreasing function of the adhesion strength. This prediction is illustrated by Supplemental Figure 3: on the fixed cell shape, the overall magnitude of the flow decreases when adhesion strength increases. Similarly, Supplemental Figure 5 shows that the flow accelerates/decelerates when the myosin strength goes up/down.

In the case where ζ is spatially constant, the resulting actin network flow patterns (the flow is slow at the front and sides, and fast at the rear) compare very well with the experimental data (compare Figures 5 and 7). If adhesion strength is high and/or myosin activity is low, then the centripetal flow of the actin network in the lab coordinate system is low, and the backward kinematic drift is faster than this flow everywhere in the cell. Under such conditions, the flow in the cell coordinate system is directed to the rear everywhere, and myosin, moving with the actin network, is effectively swept to the rear (see predicted myosin distributions in Figure 5). The predicted adhesion distribution is also high at the rear and low at the front of the cell because the flow sweeps the adhesions to the rear, similar to myosin (see predicted adhesion distributions in Figure 9). Thus, the F-actin density at the rear is damped, while along the front and sides it is distributed in a peaked way (see predicted actin distributions in Figure 9).

At low adhesion strengths and/or when myosin activity is high, the magnitude of the centripetal flow of the actin network in the lab coordinate system is greater, and at the rear it can be faster than the cell speed (especially because the latter slows down under these conditions). The net flow in the cell frame of

reference is directed inward everywhere around the boundary, so myosin, moving with the actin network, is driven inward everywhere in the cell (of course, much more so at the front, only weakly at the rear). Thus, myosin is peaked around the cell body (see predicted myosin distribution in Figure 5). Because of this more central myosin location, it pulls actin inward more evenly though the centripetal flow is still graded faster at the rear, slower at the front, it is graded now smoothly around the boundary (Figure 5). Under these conditions, emerging adhesions as well as F-actin move inward everywhere and pile up close to the cell body (Figure 9A), so around the boundary of the cell, the adhesion distribution remains low, below a threshold at which the F-actin density is damped significantly. The F-actin density stays almost constant around much of the boundary (Figure 9B).

In addition, we simulated actin network flow maps and myosin, adhesion, and actin distributions for the cases where ζ varies with adhesion density. In the case where ζ decreases with adhesion density (Supplemental Figure 8), the simulated patterns are similar to those simulated under the assumption that ζ is spatially constant and match the experimentally observed patterns. However, in the case where ζ increases with adhesion density, the simulated patterns of retrograde actin flow did not match the experimentally observed patterns (Supplemental Figures 9). Specifically, the rate of retrograde flow was nearly constant around the cell perimeter at intermediate values for ζ , in contrast to the step-like increase in flow observed experimentally (compare Supplemental Figure 9C-D, Figure 7C-D).

Stability of the cell shape

The cell shape evolves dynamically according to the graded vector sum of the outward polymerization and inward centripetal flow at the boundary. The flow, on the other hand, depends on the cell shape. The iterative procedure of evolving the coupled flow and shape showed that the stable steady fan-like shape evolves in the low adhesion case. This shape is very similar to that observed, with the aspect ratio ~ 1.5 . When the adhesion is increased to its strength in the control case, the shape elongates becoming the canoe-like and stabilizes with the aspect ratio ~ 2.5 , similar to the observed cell (Figure 11).

References

- [1] Janson LW, Kolega J, Taylor DL (1991) Modulation of contraction by gelation/solution in a reconstituted motile model. *J Cell Biol* 114: 1005–1015.
- [2] Carlsson AE (2006) Contractile stress generation by actomyosin gels. *Phys Rev E Stat Nonlin Soft Matter Phys* 74: 051912.
- [3] Rubinstein B, Fournier MF, Jacobson K, Verkhovsky AB, Mogilner A (2009) Actin-myosin viscoelastic flow in the keratocyte lamellipod. *Biophys J* 97: 1853–1863.
- [4] Mitchison T, Kirschner M (1988) Cytoskeletal dynamics and nerve growth. *Neuron* 1: 761–772.
- [5] Chan CE, Odde DJ (2008) Traction dynamics of filopodia on compliant substrates. *Science* 322: 1687–1691.
- [6] Ballestrem C, Hinz B, Imhof BA, Wehrle-Haller B (2001) Marching at the front and dragging behind: differential α v β 3-integrin turnover regulates focal adhesion behavior. *J Cell Biol* 155: 1319–32.
- [7] Fournier MF, Sauser R, Ambrosi D, Meister JJ, Verkhovsky AB (2010) Force transmission in migrating cells. *J Cell Biol* 188: 287–297.
- [8] Lee J, Jacobson K (1997) The composition and dynamics of cell-substratum adhesions in locomoting fish keratocytes. *J Cell Sci* 110 (Pt 22): 2833–2844.
- [9] Anderson KI, Cross R (2000) Contact dynamics during keratocyte motility. *Curr Biol* 10: 253–260.
- [10] Hu K, Ji L, Applegate KT, Danuser G, Waterman-Storer CM (2007) Differential transmission of actin motion within focal adhesions. *Science* 315: 111–115.
- [11] Wilson CA, Tsuchida MA, Allen GM, Barnhart EL, Applegate KT, et al. (2010) Myosin ii contributes to cell-scale actin network treadmilling through network disassembly. *Nature* 465: 373–377.
- [12] Lacayo CI, Pincus Z, VanDuijn MM, Wilson CA, Fletcher DA, et al. (2007) Emergence of large-scale cell morphology and movement from local actin filament growth dynamics. *PLoS Biol* 5: e233.
- [13] Keren K, Pincus Z, Allen GM, Barnhart EL, Marriott G, et al. (2008) Mechanism of shape determination in motile cells. *Nature* 453: 475–480.
- [14] Lee J, Ishihara A, Theriot JA, Jacobson K (1993) Principles of locomotion for simple-shaped cells. *Nature* 362: 167–171.

- [15] Schakenraad JM, Busscher HJ, Wildevuur CR, Arends J (1988) Thermodynamic aspects of cell spreading on solid substrata. *Cell Biophys* 13: 75–91.
- [16] Raucher D, Sheetz MP (1999) Characteristics of a membrane reservoir buffering membrane tension. *Biophys J* 77: 1992–2002.

Text S2

Supplemental Results

The effects of calyculin A on cell speed and area are reduced when myosin contraction is inhibited with blebbistatin

Calyculin A is a phosphatase inhibitor that is thought to indirectly increase myosin II activity [1], and we have found that keratocytes treated with calyculin A migrate at higher speeds and are smaller than control cells (see Figure 8 in the main text). To determine whether these effects are primarily due to increased myosin II activity, we treated cells crawling on glass surfaces with either blebbistatin, a myosin-II inhibitor [2], or calyculin A alone, or both blebbistatin and calyculin A (Supplemental Figure 6). We found that cells treated with blebbistatin were significantly larger and slower than control cells (average area = $424 \mu\text{m}^2$ and average cell speed = $0.20 \mu\text{m/s}$ for control cells; average area = $503 \mu\text{m}^2$, $p = 0.005$, Student's T test, and average cell speed = $0.17 \mu\text{m/s}$, $p = 0.002$, for cells treated with blebbistatin). Cells treated with calyculin A were significantly smaller and faster than control cells (average area = $332 \mu\text{m}^2$, $p = 0.001$ and average cell speed = $0.28 \mu\text{m/s}$, $p = 10^{-5}$). The effects of calyculin A on cell area and speed were greatly reduced when the cells were treated with blebbistatin for 30 minutes prior to calyculin A treatment: cells treated with both blebbistatin and calyculin A were not significantly different from control cells (average area = $405 \mu\text{m}^2$, $p = 0.44$, and average cell speed = $0.19 \mu\text{m/s}$, $p = 0.38$). Although we cannot rule out the possibility that calyculin A affects the activity of signaling proteins that regulate adhesion and motility, these results suggest that the effects of calyculin A on cell shape and speed are primarily due to increased myosin II activity.

References

- [1] Ishihara H, Ozaki H, Sato K, Hori M, Karaki H, et al. (1989) Calcium-independent activation of contractile apparatus in smooth muscle by calyculin-a. *J Pharmacol Exp Ther* 250: 388–396.
- [2] Straight AF, Cheung A, Limouze J, Chen I, Westwood NJ, et al. (2003) Dissecting temporal and spatial control of cytokinesis with a myosin ii inhibitor. *Science* 299: 1743–1747.

Table 1: Model variables.

Variable	Meaning	Dimension
t	time	sec
\vec{r}	two-dimensional coordinate	μm
s	arc length along the cell boundary	μm
$M(\vec{r}, t)$	myosin concentration	units/ μm^2
$\vec{U}(\vec{r})$	local F-actin flow velocity	$\mu\text{m}/\text{s}$
$\vec{n}(\vec{r})$	local normal unit vector to the lamellipodial edge	non-dimensional
$A(\vec{r}, t)$	adhesion concentration	non-dimensional
$a(\vec{r}, t)$	F-actin density	non-dimensional
$v(s)$	net local protrusion/retraction rate	$\mu\text{m}/\text{s}$
$V_p(s)$	local polymerization rate	$\mu\text{m}/\text{s}$

Table 2: Constant model parameters.

Parameter	Meaning	Value
M	total myosin	55 units
D_M	effective myosin diffusion coefficient	$0.8 \mu\text{m}^2/\text{s}$
D_A	small adhesion diffusion coefficient	$0.2 \mu\text{m}^2/\text{s}$
D_a	small actin diffusion coefficient	$0.2 \mu\text{m}^2/\text{s}$
μ	shear F-actin viscosity	$2 \text{ kPa}\times\text{s}$
μ_b	bulk F-actin viscosity	$100 \text{ kPa}\times\text{s}$
S_A	adhesion assembly rate	1 unit/50 s

Table 3: Model parameters dependent on adhesion strength.

Parameter	Meaning	Low	Medium	High
ζ [nN \times s/ μm^4]	adhesion drag coefficient	0.04	0.2	20
ϑ [non-dim]	flow-coupling coefficient	0.9	0.4	0.2
γ [1/s]	adhesion disassembly rate	1/50	1/150	1/250
v [1/s]	actin disassembly rate	1/50	1/50	1/100
α [1 unit $\times\mu\text{m/s}$]	F-actin assembly rate	2	0.4	0.4
M_0 [non-dim]	threshold myosin density for myosin-mediated actin depolymerization	140	20	200
A_0 [non-dim]	threshold adhesion density for adhesion-dependent inhibition of actin polymerization	0.01	1	0.2

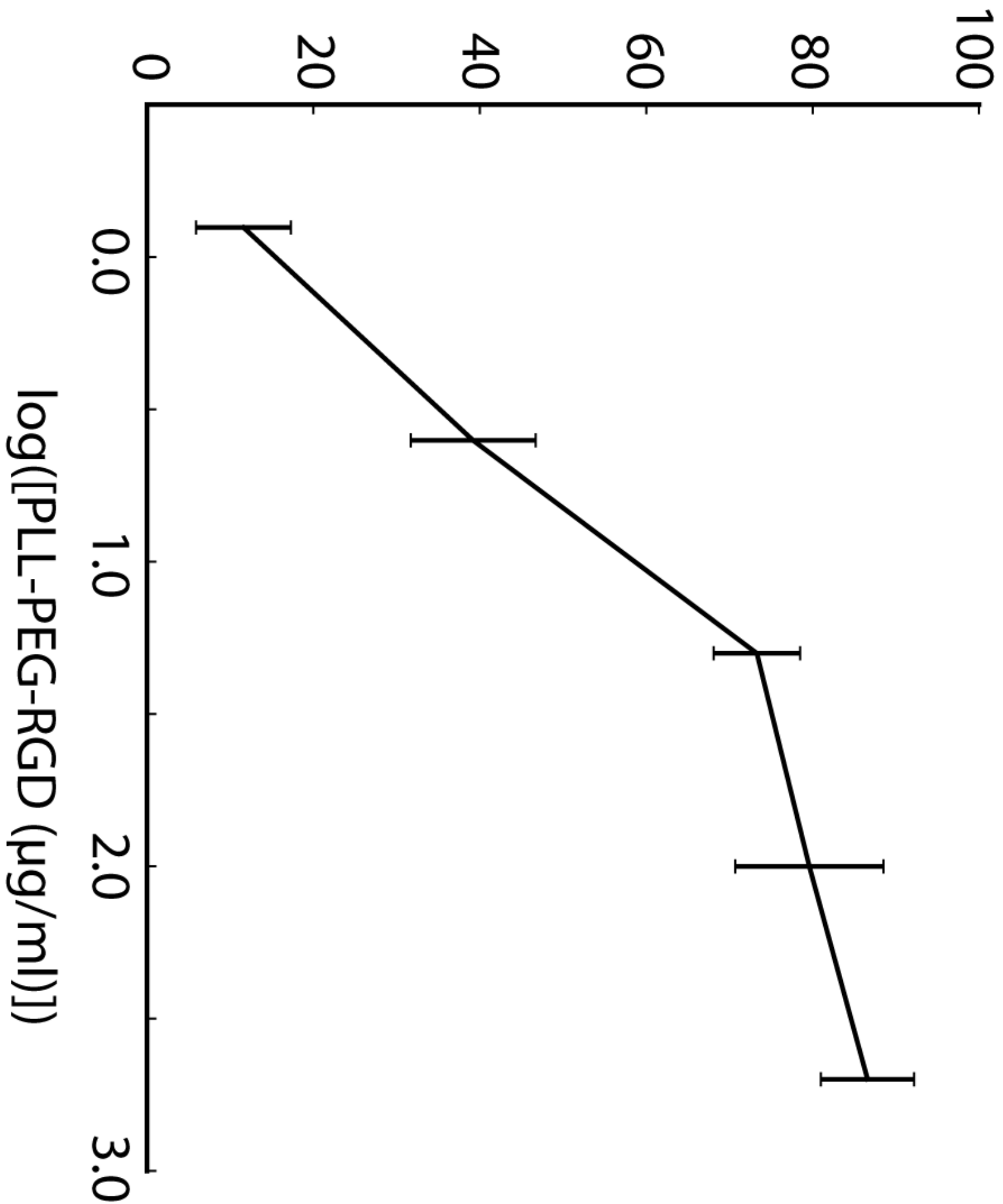
Table 4: Model parameters dependent on myosin strength.

Parameter	Meaning	Blebbistatin	Control	Calyculin
k [pN]	myosin force coefficient	45	100	130

Table 5: Model parameters dependent on adhesion and myosin strength.

Param.	Meaning	Cont Low	Cont Med	Cont High	Caly Low	Caly Med	Caly High	Bleb Low	Bleb Med	Bleb High
\bar{A} [μm^2]	cell area	300	460	513	297	383	397	470	434	456
V_{cell} [$\mu\text{m}/\text{s}$]	cell speed	0.12	0.20	0.08	0.16	0.22	0.08	0.10	0.15	0.16

percent of cells attached
after centrifugation

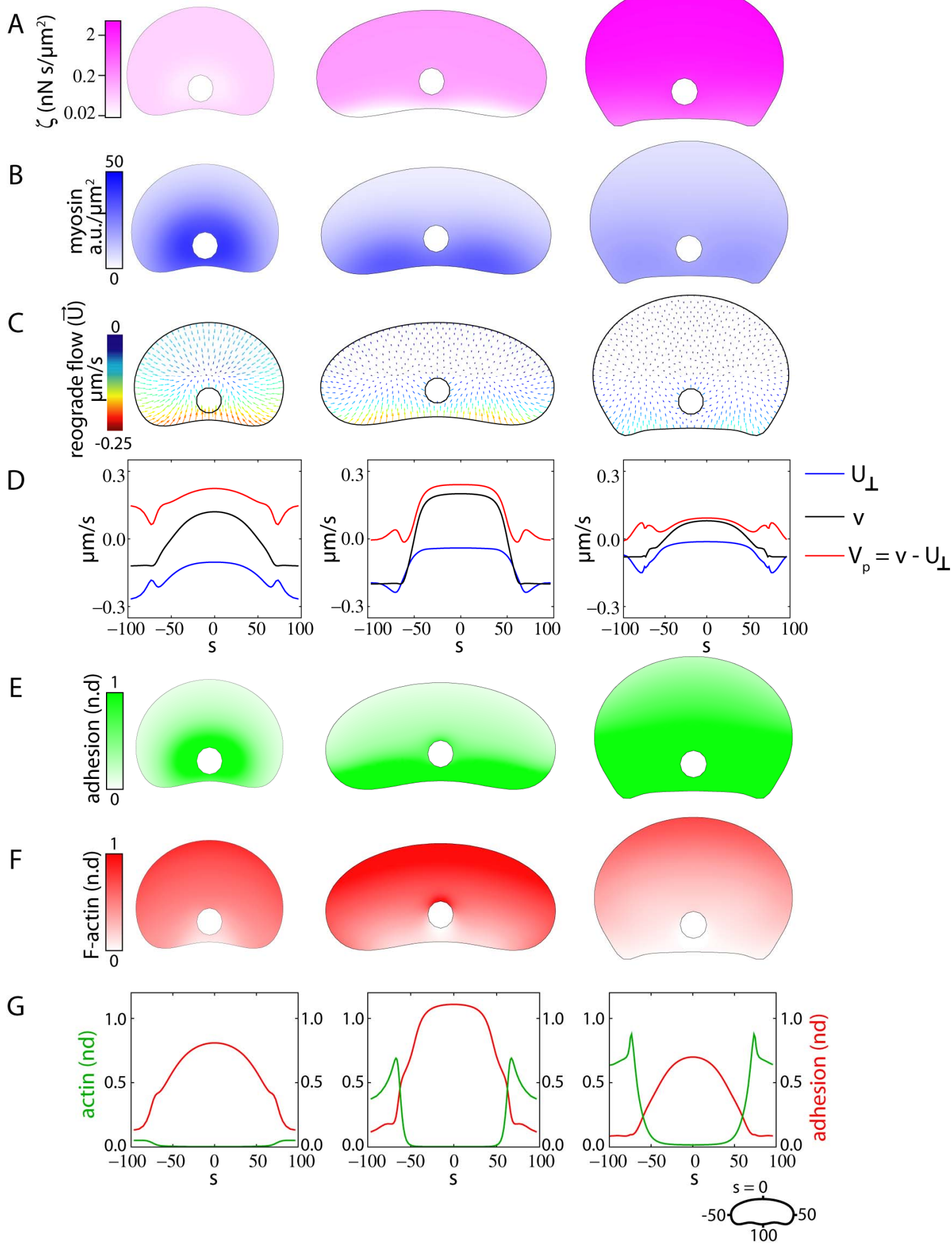


adhesion strength

low

medium

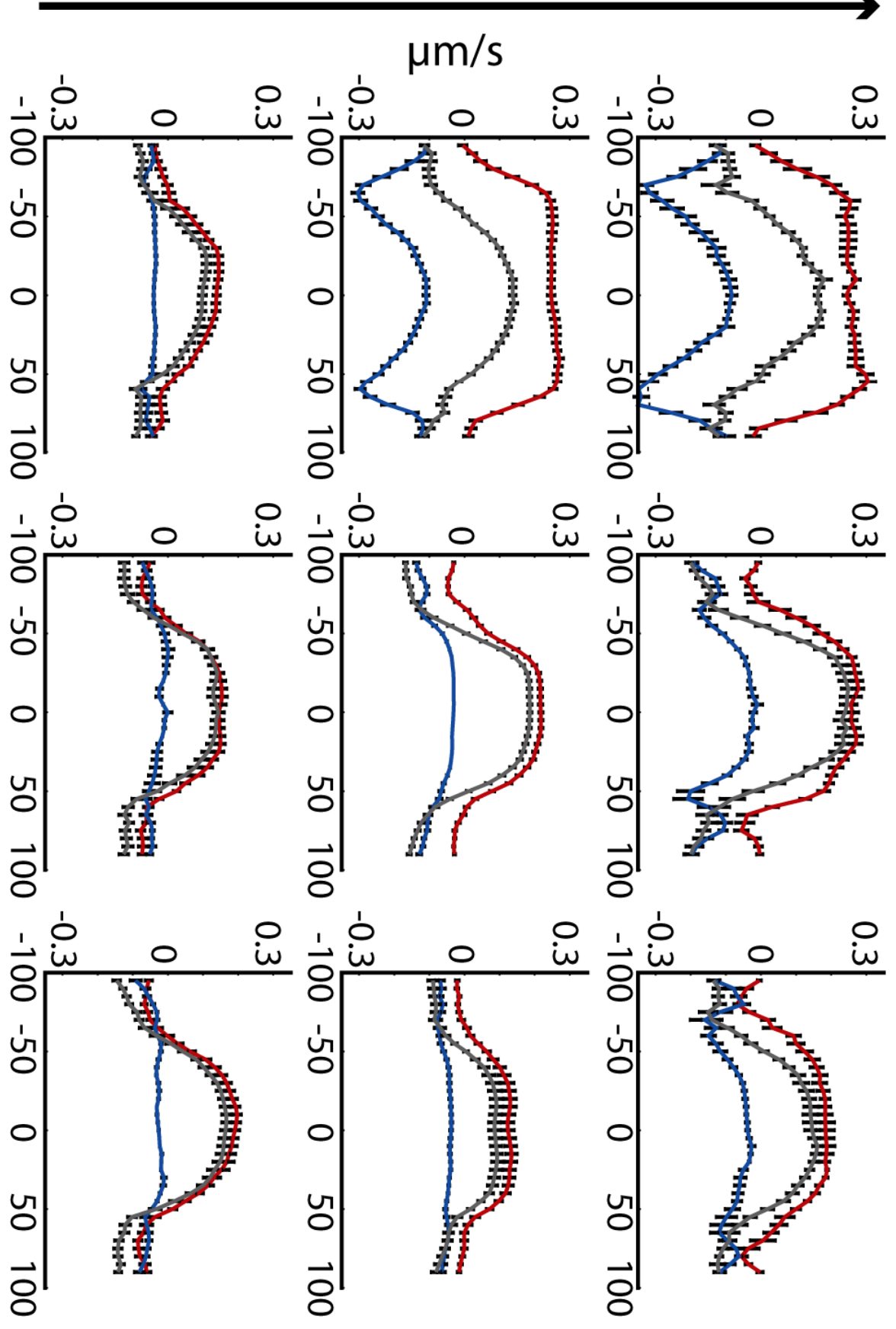
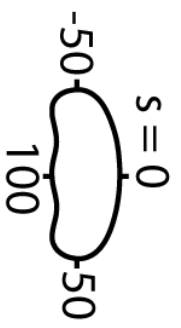
high



A

myosin activity

blebbistatin control calyculin A

 $\mu\text{m/s}$ 

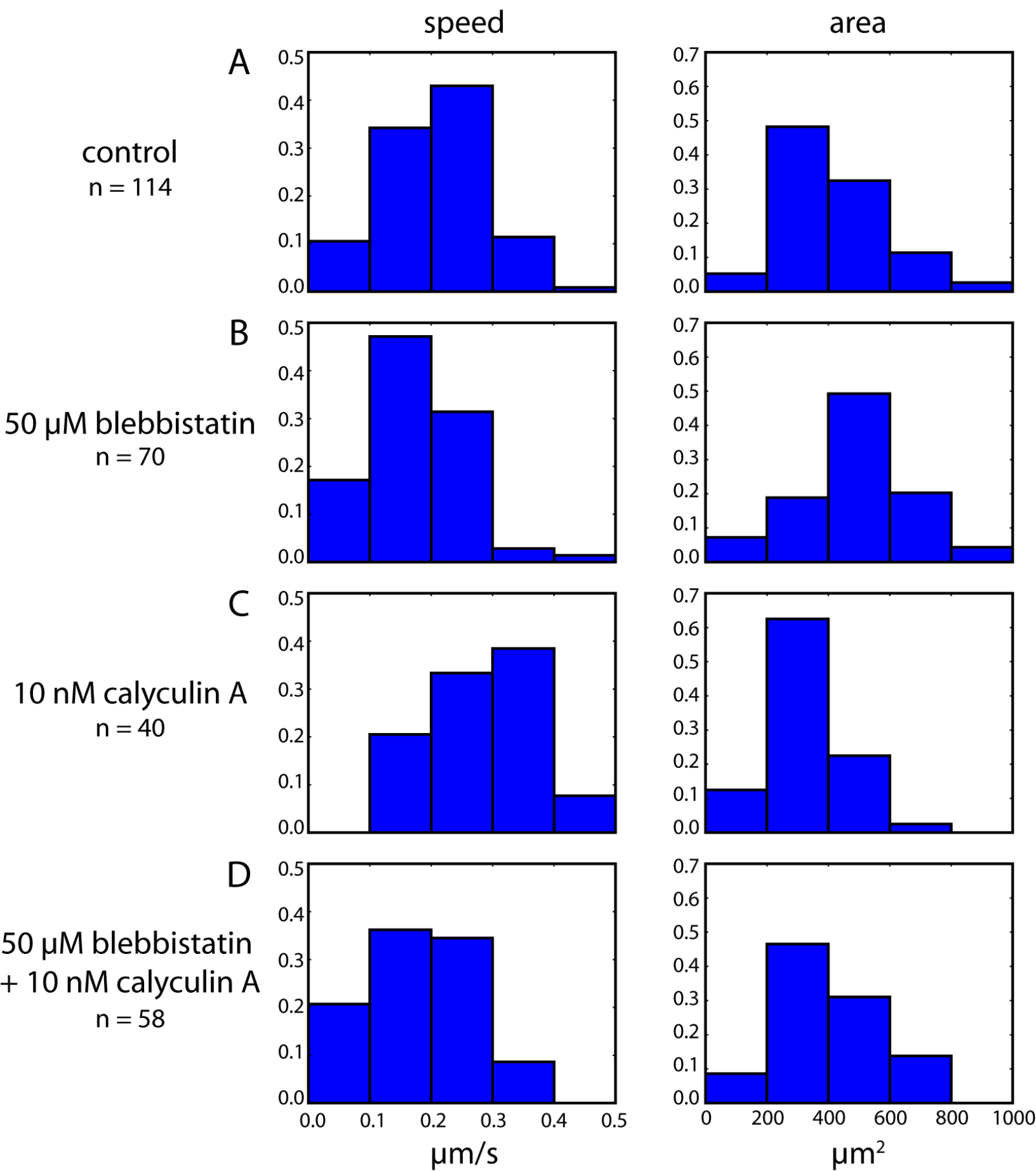
low

medium

high

adhesion strength

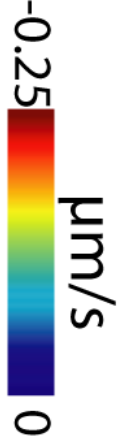
— actin polymerization — actin retrograde flow — actin polymerization + retrograde flow



simulated actin retrograde flow

myosin activity

low $k = 45 \text{ pN}$ medium $k = 100 \text{ pN}$ high $k = 130 \text{ pN}$



low

$\zeta = 0.04 \text{ nN s}/\mu\text{m}^4$

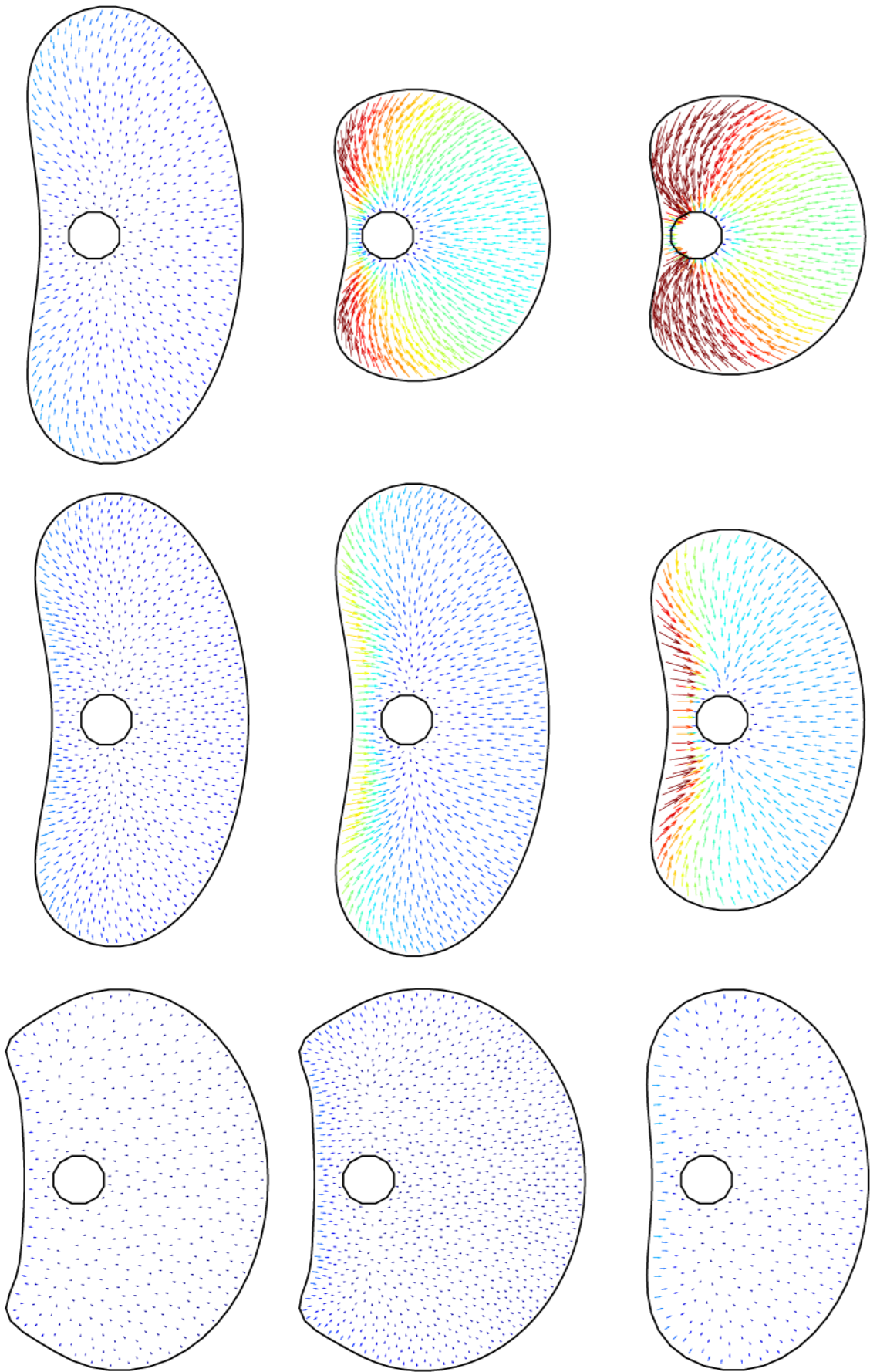
medium

$\zeta = 0.20 \text{ nN s}/\mu\text{m}^4$

high

$\zeta = 20 \text{ nN s}/\mu\text{m}^4$

adhesion strength

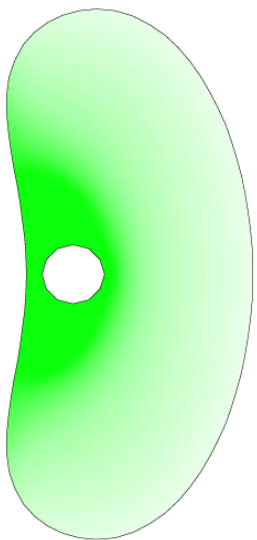


adhesion strength

low

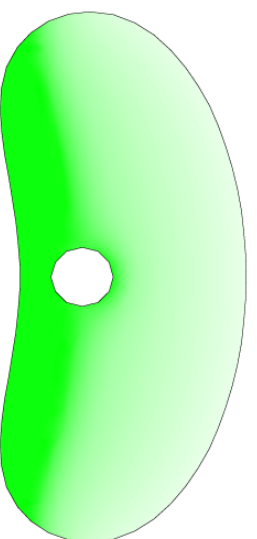
$$\zeta = 0.04 \text{ nN s}/\mu\text{m}^4$$
$$V_{\text{cell}} = 0.12 \mu\text{m}/\text{s}$$

adhesion (n.d.)



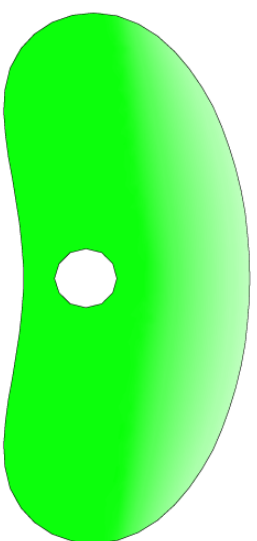
medium

$$\zeta = 0.2 \text{ nN s}/\mu\text{m}^4$$
$$V_{\text{cell}} = 0.20 \mu\text{m}/\text{s}$$



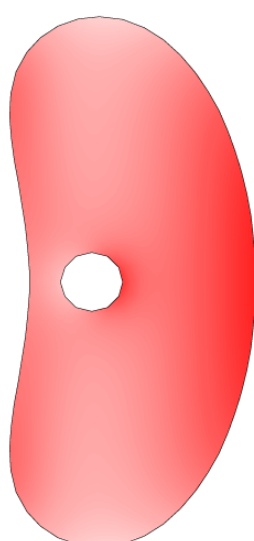
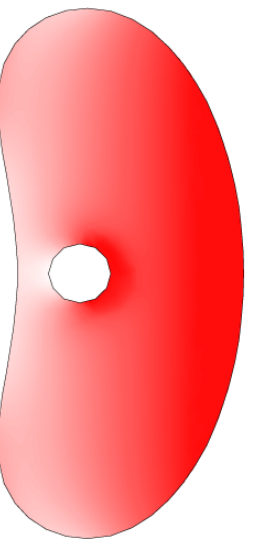
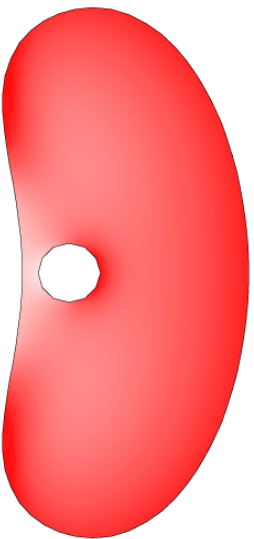
high

$$\zeta = 20 \text{ nN s}/\mu\text{m}^4$$
$$V_{\text{cell}} = 0.08 \mu\text{m}/\text{s}$$



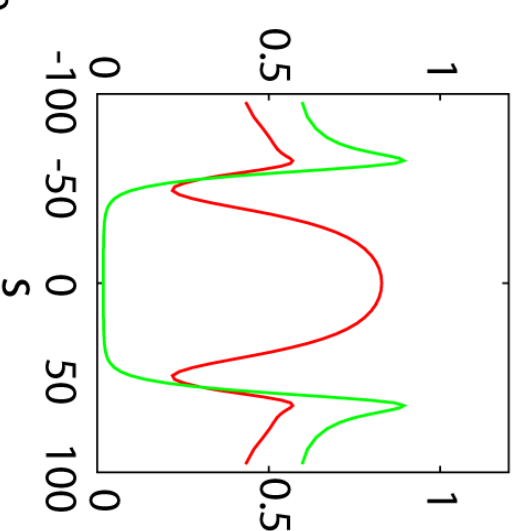
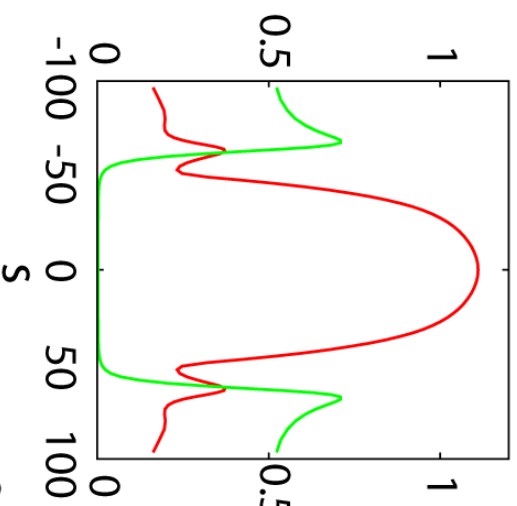
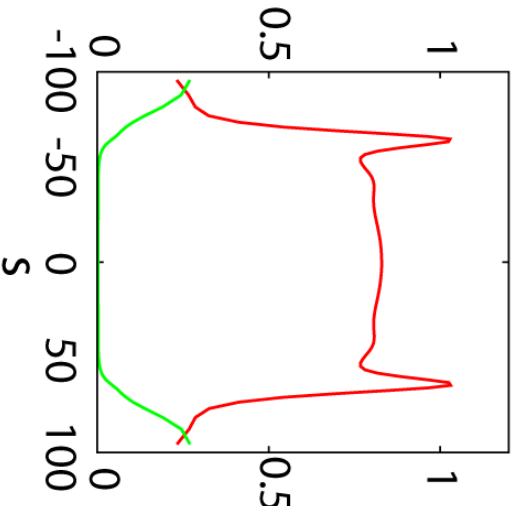
B

F-actin (n.d.)

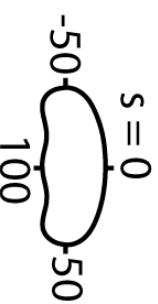


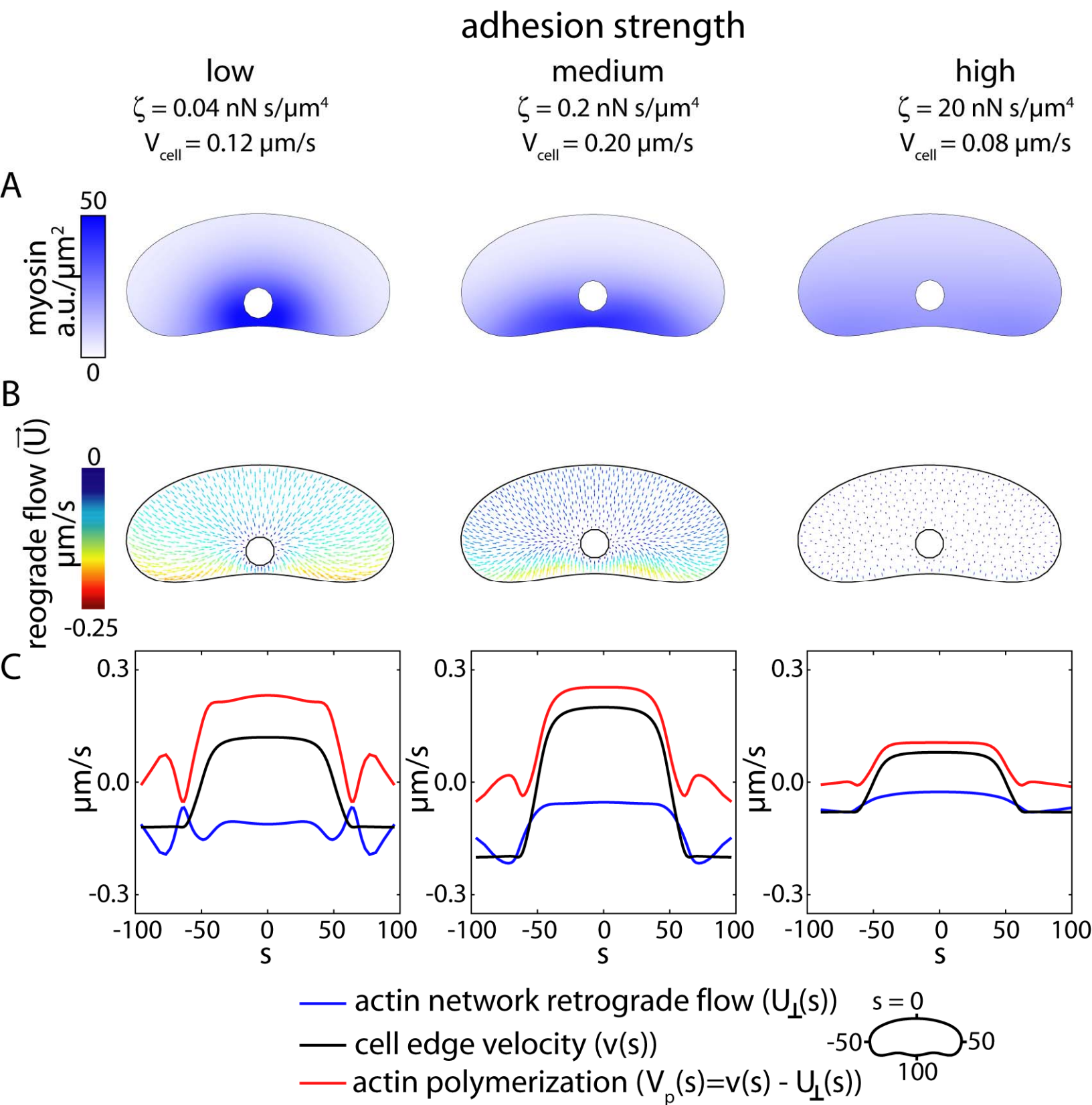
C

actin (n.d.)

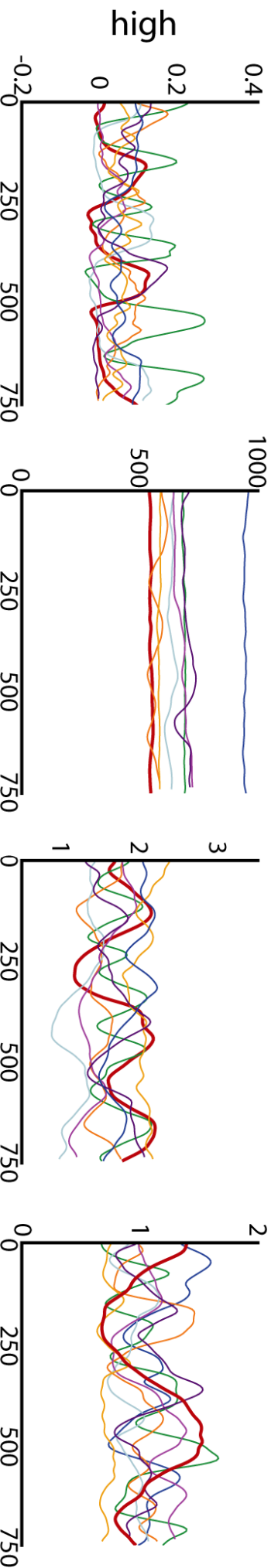
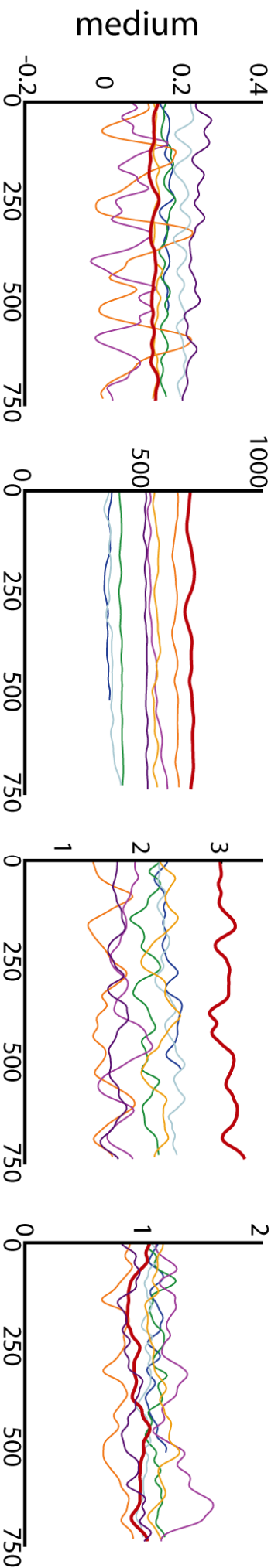
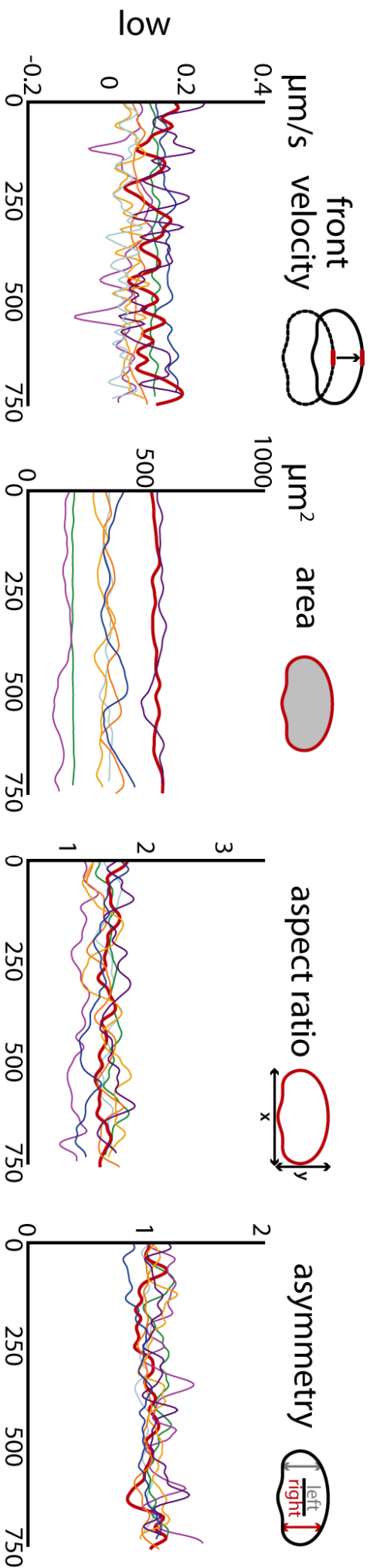


adhesion (n.d.)





adhesion strength



seconds

adhesion strength

low

medium

high

